

This is the peer reviewed version of the following article:

Deformation Sequence and Paleofluids in Carbonate Buckle Folds Under Transpression (Pag Anticline, External Dinarides, Croatia) / Lucca, A.; Mittempergher, S.; Succo, A.; Bistacchi, A.; Meda, M.; Storti, F.. - In: TECTONICS. - ISSN 0278-7407. - 42:10(2023), pp. 1-38. [10.1029/2023TC007781]

Terms of use:

The terms and conditions for the reuse of this version of the manuscript are specified in the publishing policy. For all terms of use and more information see the publisher's website.

29/04/2024 17:43

(Article begins on next page)

DEFORMATION SEQUENCE AND PALEOFLUIDS IN CARBONATE BUCKLE FOLDS UNDER TRANSPRESSION (PAG ANTICLINE, EXTERNAL DINARIDES, CROATIA)

Lucca A.¹, Mittempergher S.², Succo A.¹, Bistacchi A.³, Meda M.⁴ and Storti F.¹

1. Università degli Studi di Parma, Dipartimento di Chimica, Scienze della Vita e della Sostenibilità Ambientale, NEXT, Natural and Experimental Tectonic Research Group, Parco area delle Scienze 157/A, 43124 Parma, Italy.
2. Università degli Studi di Modena and Reggio Emilia, Dipartimento di Scienze Chimiche e Geologiche, via Giuseppe Campi 103, 4112 Modena, Italy.
3. Università degli Studi di Milano-Bicocca, Dipartimento di Scienze dell'Ambiente e della Terra, Piazza della Scienza 4, 20126 Milano, Italy.
4. ENI Spa, Natural Resources, San Donato Milanese, Italy.

ABSTRACT

Contractional deformation structures at the front of transpressional orogens display complex three-dimensional geometries deviating from the interpretative templates commonly applied in thrust belts. Accordingly, detailed constraints on deformation patterns and associated paleofluid circulation are desirable, especially for fracture geometry and permeability predictive purposes. The Pag anticline, which is located in the Dinaric fold and thrust belt, provides an appropriate field site for studying fold- and fault-related deformation structures in a transpressive setting. We performed a multiscale structural analysis together with petrographic and stable isotope characterization of the deformation-related calcite cements. Structural mapping suggests that the Pag anticline is a detachment fold developed mainly by buckling, since large-scale thrust faults are absent. Fold tightening in a transpressive setting produced a complex deformational structure including two sets of N-S right-lateral and E-W left-lateral late-stage strike-slip fault sets trending oblique to the NW-SE fold axis. The pre-folding deformation pattern includes incipient normal faults likely related to the forebulge stage, veins and stylolites coherent with NE-SW layer parallel shortening contraction in a strike-slip regime, and metric to decametric scale conjugate thrusts coherent with layer parallel shortening in a compressive regime. Buckle folding preceded propagation of a series of accommodation structures during fold tightening. Petrographic and isotopic data indicate meteoric alteration of the Cretaceous platform carbonates in the prefolding stage, likely due to forebulge subaerial exposure. Layer parallel shortening and early syn-folding veins involved formational fluids resulting from mixed marine and meteoric fluids during folding at shallow burial conditions. Eventually, meteoric fluid infiltrated again along strike-slip faults, acting as cross-formational conduits in the postfolding stage.

1. INTRODUCTION

The study of exhumed folds that developed at shallow depths in foreland basins can provide qualitative and quantitative information useful for the optimal exploitation of underground resources and for the mitigation of seismic hazard, both natural and induced, in regions that are commonly characterized by high population density. Buried folds in foreland basins also provide suitable sites for storing gas at depth, including CO₂ sequestration (e.g., Urych et al., 2022) and

This article has been accepted for publication and undergone full peer review but has not been through the copyediting, typesetting, pagination and proofreading process, which may lead to differences between this version and the [Version of Record](#). Please cite this article as [doi: 10.1029/2023TC007781](https://doi.org/10.1029/2023TC007781).

power-to-gas storage solutions (e.g., [Lehner et al., 2014](#)). Effective exploitation of fluid storage potential in buried folds strongly benefits from a detailed knowledge of the structure geometries, fracture distribution and fluid mobility patterns inferred from suitable field analogues. Reliable 3D reservoir geomodels typically result from the combination of hard data, conceptual models (soft data), and the imaging of the subsurface ([Cannon, 2018](#)). The first two components require input information from the study of field analogues ([Howell et al., 2014](#)).

Fold evolution and kinematics in foreland basin systems is driven by multiple factors, including the mechanical properties of the folded multilayers ([Corbett et al., 1987](#); [Gross, 1993](#); [Fischer & Jackson, 1999](#); [Wennberg et al., 2006](#); [Tavani et al., 2008](#); [Lacombe, 2010](#)), the presence of inherited, pre- or syn-orogenic fault zones (e.g. [Butler, 1989](#); [Tavarnelli, 1996](#); [Storti et al., 2018](#); [Tavani et al., 2018](#)), and the ratio between tectonic uplift and foreland basin syntectonic sedimentation rates ([Storti & Salvini, 1996](#)) and the relationships of folds with underlying faults (e.g. [Suppe, 1983](#); [Tavani et al., 2006](#)). In the last decades, fold trains in thrust and fold belts have mostly been interpreted as fault-related, neglecting the contribution of buckle folding to the regional contraction ([Suppe, 1983](#); [Jamison, 1987](#); [Erslev, 1991](#); [Shaw et al, 2005](#)). Kinematic models of fault-related folds have been extensively applied for estimating the displacement accommodated along blind thrusts for seismic hazard assessment purposes ([Dolan & Avouac, 2007](#)), although analogue and numerical modeling, and field studies suggest that a potentially large component of fold growth might be attributed to buckling in addition to slip on the underlying fault ([Johnson, 2018](#); [Butler et al., 2018, 2020](#); [Mazzoli et al., 2022](#)). A reliable interpretation of the structural style and partition of the contraction between faulting and folding is therefore crucial for estimating the size of seismogenic sources in thrust and fold belts.

An additional factor affecting the structural complexity of thrust and fold belts is the occurrence of components of oblique convergence (e.g., [Teyssier et al., 1995](#)). In a transpressional regime, the three-dimensional folding-related deformation patterns can significantly differ from the deformation structures expected in purely compressive settings ([Stearns, 1968](#); [Cooper, 1992](#); [Storti & Salvini, 2001](#); [Lacombe et al., 2012](#); [Tavani et al., 2015](#)), being typically characterized by additional complexity due to the combination of coaxial and non-coaxial strain ([Linzer et al., 1995](#); [Leever et al., 2011](#); [Ellero et al., 2012](#)). In such cases, availability of three dimensional templates from appropriate field analogues is certainly beneficial for better understanding fault-fold kinematics for academic, economic, and societal purposes.

Different deformative mechanisms produce distinctive patterns of fold- and fault-related fracturing, therefore controlling the temporal evolution of fluid circulation in thrust belts. Important information on fluid-rock interactions and fluid flow at depth are provided by the study of cements associated with deformation structures ([Laubach et al., 2010](#); [Beaudoin et al., 2022](#) and references therein), which add further constraints on fluid origin and circulation paths, and the relative chronology of deformation (e.g., [Roure et al., 2005](#); [Storti et al., 2018](#); [De Graaf et al., 2019](#); [Berio et al., 2021](#)).

Here we present the analysis of fold structure, fault-fold interplay, and folding-related mesoscale deformation structures exposed in the Pag anticline, in the northwestern sectors of the External Dinarides of Croatia. We interpret the Pag anticline as a detachment fold, developed mainly by buckling, and crosscut by a late- to post-folding pervasive network of strike-slip faults producing an overall rotation coherent with the dextral oblique convergence in the region. Petrographic and isotopic characterization of vein cements indicate that deformation occurred at relatively shallow

This article is protected by copyright. All rights reserved.

depth, with an opening of the system to cross-formational ingress of meteoric water in the late-to post-folding strike-slip faulting stage. Based on this multidisciplinary dataset, we propose an evolutionary model for the Pag anticline, integrating deformation stages with fluid circulation pathways. Fracturing and fracture sealing produce also complex feedbacks with the evolution of effective stresses in tight carbonates, since confined, low-permeability fluid systems are potentially prone to the syn-tectonic buildup of fluid overpressures (e.g., Cox, 2010; Cerchiari et al., 2020).

2. GEOLOGICAL SETTING

The Dinarides are a NW-SE striking, SW-verging fold and thrust belt belonging to the Alpine-Himalayan orogenic system (e.g., McKenzie, 1978; Dewey et al., 1989; Rosenbaum & Lister, 2002). The Dinarides are delimited to the N by the Periadriatic fault, to the NE by the Pannonian Basin, to the S by the Shkoder-Pec lineament and to the SW by the Adriatic foreland (Figs. 1a-b). The Dinaric orogen developed by subduction and indentation of the Adriatic microplate towards NE into the European plate, which caused the closure of the Balkan Neotethys and eastward escape of Tisza and Eastern Alps (Fig. 1b) tectonostratigraphic domains towards the Carpathian paleo-embayment, from upper Jurassic times onward (Schmid et al., 2008; Handy et al., 2015). The southwest-vergent Dinaric nappe stack is composed of the Adria passive margin succession, which includes, from SW to NE, the Mesozoic Adriatic carbonate platform (ACP; consisting of the Dalmatian and the High Karst tectonic domains, Vlahović et al., 2005), the transitional marine succession of the Pre-Karst and the deep marine succession of the Internal Dinarides. The Western Vardar Ocean ophiolitic sequence and the Sava magmatic arc are juxtaposed above the former ACP units and define the suture zone between Adria and the Europe-derived tectonic blocks (Fig. 1b; Herak, 1999; Dragičević and Velić, 2002). In the Albanides, Montenegro and southern Dalmatia, the Dalmatian and the High Karst tectonic domains are separated by the Budva inter-platform through which narrows and is not outcropping from Split towards the north (Gusić and Jelaska, 1993; Tari, 2002; Velić et al., 2002; Vlahović et al., 2002; Velić et al., 2015).

The High Karst domain was underthrust in Paleogene times by the most external tectonic unit of the Dinarides fold and thrust belt, the Dalmatian domain, bounded to the SW by the Dinarides deformation front (Fig. 1b; e.g., Schmid et al., 2008). The High Karst domain is composed of limestones and dolostones of the Dinaric carbonate platform sequence that underwent erosion due to subaerial exposure during the forebulge stage of the subducting Adria continental margin (Tari-Kovačić, 1997; Tišljarić et al., 2002; Brlek et al., 2014). Late Cretaceous to middle Eocene sedimentary hiatuses are exposed in the northern Adriatic Islands (Pamić et al., 1998) and are unconformably covered by foraminiferal limestones marking the initiation of the “underfilled trinity” foredeep sequence (Sinclair, 1997) induced by flexural loading of Adria below the advancing Dinaric thrust belt (Ćosović et al., 2004; Babić and Zupanić, 2016; Ćosović et al., 2017). The foraminiferal limestones are covered by few meters of Globigerina marls (“transitional beds”) and by pelites and sandstones of the Dalmatian flysch, deposited in tectonically confined proximal basins (Piccoli and Proto Decima, 1969; Babić et al., 1993; Tari-Kovačić and Mrinjek, 1994; Bennett et al., 2008). The ages of the syntectonic “underfilled trinity” span from Lutetian-Bartonian in the NW (Pag and Rab Islands), up to early Oligocene in the SE (Split). Two parautochthonous syntectonic clastic sequences deposited in the area during Paleogene: (i) the Promina alluvial deposits (Mrinjek, 1993; Babić and Zupanić, 2007) and (ii) the Eocene-Oligocene Velebit (or Jelar) breccia, interpreted to be the product of multiple stages of subaerial thrusting and erosional

unroofing and to possibly represent the proximal equivalent of the Promina deposits. The latter unconformably overlay the Dalmatian flysch, testifying for an articulated wedge-top depositional system and a general regressive trend during southwestward directed folding and thrusting of the Dinaric High Karst (Figs. 1b-c; Babić and Zupanić, 2008).

Paleomagnetic data indicate no net rotation between Adriatic and European plates during the Eocene thrusting and folding stage (Márton et al., 2010; Márton et al., 2014; 2022). At the beginning of Oligocene, Adria changed from a northwestward to a more westward compression direction. Therefore, the Periadriatic fault accommodated dextral strike-slip deformation in between Adria and Europe. The European slab underwent delamination or break-off. These tectonic events possibly led to dextral strike-slip tectonics and delamination of the Adriatic lithosphere below parts of the central and northern Dinarides (Handy et al., 2015; Belinić et al., 2021). Calc-alkaline magmatism in the Internal Dinarides has been related to asthenospheric upwelling and partial melting of the Adriatic crust, that eventually led to extension in the Pannonian Basin (Mandić et al., 2012). Moreover, peneplanation surfaces and coastal terraces as high as 600 m a.s.l., are well preserved along the Velebit Mts., northern and central Dalmatia and are interpreted to be the result of uplift due to isostatic rebound in the High Karst domain, possibly induced by delamination of the Adriatic crust (Balling et al., 2021a). The External Dinarides were affected by 20° to 25° counterclockwise rotation with respect to stable Europe during Oligocene times. The Dalmatian domain and undeformed Adria underwent additional 5° to 10° CCW rotation since Miocene to present (Márton et al., 2003; Ilić and Neubauer, 2005; Ustaszewski et al., 2008; Márton et al., 2010; De Leeuw et al., 2012; Márton et al., 2014; Šumanovac et al., 2017; Le Breton et al., 2017).

The Neogene tectonic scenario was characterized by indentation of Adria in the Alps accompanied by eastward escape of the Eastern Alps tectonic unit (Ustaszewski et al., 2008). The northward movement of Adria was accommodated in the northern and central Dinarides by localized strike-slip deformation along major dextral, NNW-SSE striking fault systems (Merlini et al., 2002; Picha, 2002; Placer et al., 2010; Van Unen et al., 2019) that often-reactivated Mesozoic extensional faults of the Adria passive margin, produced by E-W to ENE-WSW extension during the Neo-Tethys rift in the Jurassic (Burberry and Swiatlovski, 2016). During the early to middle Miocene, freshwater lacustrine sediments accumulated in intramontane basins in the High Karst and Pre-Karst domains (Dinaric Lake System). These depocenters are interpreted either as pull-apart basins related to the Oligocene dextral strike-slip deformation, followed by Pliocene NE-directed backthrusting of the Dinarides (Hrvatovic, 2005), or as basins that formed during a Neogene NE-SW extensional phase related with the development of the Pannonian basin, followed by a right-lateral transpressional deformation with N-S directed σ_1 (Ilić & Neubauer, 2005; Faivre, 2007; van Unen et al., 2019). The main Post-Oligocene dextral strike-slip fault systems in the External Dinarides include the Split-Karlovac Fault, dissecting the High Karst Unit, and the NE Adriatic Fault (NEAF; Korbar, 2009). The former splays from the NEAF in a N-S direction moving northward the town of Split. The NEAF runs along the Croatian coastline from Montenegro in the southeast up to the Iulian Alps in Italy, crossing northern Dalmatia and Istria onshore. The NEAF is interpreted to be an inherited early Mesozoic extensional fault system reactivated with right-lateral transpressional kinematics and interacting with Cenozoic thrust fault systems of the Velebit Mts. antiformal stack (Figs. 1b-c-d; Kovacs et al., 2007; Korbar, 2009).

The complex structure of the region (**Fig. 1c**) and the occurrence of thick clastic deposits of debated origin, named Velebit breccias, unconformably cover the pre-Oligocene contractional structure of the Velebit Mountains, led to different interpretations of the subsurface structure of the Lika region and the northern Dalmatian area: a) the Velebit Mts. area is a crustal scale antiformal stack and northern Dalmatia represents passive roof folds of the stack (Korbar, 2009); b) the Velebit Mts. and the northern Dalmatia constitute the hanging wall of a foreland-ward dipping passive roof thrust system of a large antiformal stack having its core in the Lika region (Chorowicz, 1974; Balling et al., 2021b); c) the Velebit Mts. and the Lika region constitute the hanging wall of a major out-of-sequence thrust and the northern Adriatic Islands are located in the footwall (Tari-Kovačić and Mrinjek, 1994; Prelogović et al., 1998). The cross-sectional geometry illustrated in **Fig. 1d**, according to interpretation (c), is based on Grandić et al., 2002 and shows the Velebit Mts. thrust stack characterized by thick-skinned deformation, possibly interacting with the dextral transpressive NEAF, and passing seaward to a thin-skinned imbricate fold train. In this interpretation, thrusting and folding in the external fold train is favored by evaporitic layers of Late Jurassic age, whose occurrence is restricted to the northern Dalmatian area according to well data (Đurasek et al., 1981; Korbar, 2009). The younger crustal-scale Neogene strike-slip deformation is well evident, particularly by the broad transpressive crustal structure occurring to the NE of the Velebit Mts. antiformal stack, which emanates from the Split-Karlovac Fault (**Fig. 1d**).

Neotectonic activity in the northern and central external Dinarides produces low intensity seismicity that highlights thrust fault arrays in northern Dalmatia interacting with the NEAF and other strike-slip and transpressional faults at the toe of the Velebit Mts. antiformal stack (Kuk et al., 2000). Seismic events with M_w higher than 4.0 were recorded to the north in Kvarner area and to the south along the Split-Karlovac fault near the town of Split, while no comparable seismic activity was recorded but were not recorded in northern Dalmatia and Adriatic islands (ISIDE, 2007). Earthquake focal mechanics and geodetic measurements indicate that the principal contractional axis strikes NNE-SSW to N-S and the contraction rate is 0.2-0.3 mm/y (Kastelić and Carafa, 2012; Ivančić et al., 2018; Pavasović et al., 2021). The area is characterized by extremely low geothermal gradients of 15 °C/km and lower in the upper part of the crust (top 3 km): oil exploration wells recorded temperatures of 30-40 °C at 3 km depth in the External Dinarides (Grandić & Kolbah, 2009; Kovačić, 2013).

3. METHODS

The geological map is based on field surveys integrated with the interpretation of high-resolution satellite images available from the Bing portal (<https://www.bing.com/maps>) and the geoportal of the Croatian Geodetic Service (<https://geoportal.dgu.hr/>). Field surveys were conducted on printed aerial photographs, or on GPS equipped tablets, mainly at the 1:5,000 scale, and locally at the 1:2,000 scale (see Mitterpergher et al., 2019). The geological cross-sections were constructed using the MOVE suite (Petroleum Experts Ltd) to combine information from our field data, measured stratigraphic sections and published geological maps (Majcen et al., 1976; Mamužić and Sokač, 1973; Sokač et al., 1976; Mitterpergher et al., 2019).

4,990 structural data were collected in 54 structural stations. We acquired measurements of orientations, kinematics, and crosscutting relationships of all the deformation structures at each station. Deformation structures are divided in four groups: (a) background deformation structures

include elements which were collected far from fault damage zones; their attitude is referred to bedding and to the anticline axis trend (e.g., bed parallel, axial parallel or longitudinal, axial orthogonal or transversal); (b) deformation structures related with soft-sediment faults; (c) thrust related deformation structures; (d) strike-slip fault-related deformation structures. The measured structural elements include attitude and kinematics of faults, and orientation of veins and pressure solution surfaces. Stereographic projections were made using the Daisy3 software (Salvini, 2019). Field station positions and raw data are provided in the supplementary material tables S1 and S2.

We attempted to calculate the paleostress field of the Pag anticline through the inversion of fault slip, veins, and stylolite data (e.g., Angelier and Mechler, 1977; Delvaux and Sperner, 2003). Stress inversion is based on three assumptions: (i) homogenous stress tensor, (ii) infinitesimal strain and (iii) no dynamic effects of deformation (Sperner and Zweigel, 2010). The calculated tensor parameters are the orientation of the three principal stresses $\sigma_1 > \sigma_2 > \sigma_3$ (with compressive stresses >0) and the stress tensor shape ratio $R = (\sigma_2 - \sigma_3)/(\sigma_1 - \sigma_3)$ (Angelier, 1990). We used the Win-Tensor program for paleostress analysis following the method of Delvaux and Sperner, 2003. We calculated then the mean stress tensors for each deformation stage. To test the homogeneity and coherency of mean stress tensors, we applied a bootstrap modelling implemented in a custom Matlab® script (Figs. 15c, d, e; Bistacchi et al., 2012; Traforti et al., 2018). Bootstrap modelling assumes that the statistical relationships between a sample (mean stress tensor from field data) and the underlying population (the true stress tensor) should have the same form as those between a random resampling and the sample itself.

115 thin sections were cut from rock specimens sampled in the study area. Each sample was cut in two slabs, one of which was stained with Alizarin Red S and potassium ferricyanide to discriminate the different carbonate minerals including calcite and dolomite and their iron-rich equivalents (Dickson, 1966). The remaining slabs were used to obtain standard 30 μm thin sections. Petrographic optical analyses were performed with a Zeiss Axioplan 2 microscope. Moreover, cold cathodoluminescence (CL) microscopy was performed by a Technosyn 8200 Mark II cold CL stage, mounted on a LEICA DM2700P optical microscope, at 10 kV and 256 μA gun current. Calcite cement types are indicated by different acronyms for host rocks (HR), intergranular (C) and vein cements (V) and followed by suffixes representing the hosting formations. Vein cements with no suffix are hosted in undifferentiated Cretaceous limestones. Numbers from 1 to 3 indicate stages of progressive vein cement development and refer to pre-, syn- and post-folding stages, respectively. V_T calcite cement is hosted in thrust-related veins.

Following petrography and cathodoluminescence analyses, oxygen and carbon stable isotope ratios were determined on 289 selected samples of host rocks and cements. Stable isotope ratios are reported in ‰ notation relative to the V-PDB standard (Vienna Pee Dee Belemnite). 210 sub-samples of cements and host rocks were drilled directly from thin sections with an ESI New Wave Research Micromill with sub-micron step resolution and a milling chuck speed ranging from 1,200 rpm to 35,000 rpm. An additional of 43 sub-samples were drilled from rock slabs using a dental drill with 500 μm wide drill bits. For the isotopic analysis of each sample, 150-200 μg of carbonate powder was loaded into a GasBenchII autosampler, interspaced with three different reference materials (NBS18, NBS19 and MAB99). After helium flushing, 100% orthophosphoric acid was added at 25 °C and reacted at 72 °C. Resulting gases were analyzed automatically using a Thermo Finnigan Delta V+ mass spectrometer. 40 peaks, in 10 steps, were measured for each sample. Each

sample was analyzed twice so the data uncertainty is $\pm 0.10\%$ and $\pm 0.15\%$ for $\delta^{13}\text{C}$ and $\delta^{18}\text{O}$, respectively.

4. GEOLOGY OF THE PAG ANTICLINE

4.1 Stratigraphy

The Pag Island exposes the Upper Cretaceous (Cenomanian to Coniacian) rudist-bearing platform carbonate succession of the Adriatic Carbonate Platform (ACP; Vlahović et al., 2005), namely, the informal lithostratigraphic units known as Milna formation (fm. hereafter; Cenomanian), Sveti Duh fm. (Cenomanian-Turonian), and Gornji Humac fm. (Coniacian) (Figs. 2-3) (Gušić & Jelaska, 1990; 1993). The Milna fm. mainly consists of a sequence of shallowing upward cycles of intertidal limestones with dominant supratidal facies, with stromatolite-rich beds, microbial laminites and oxidized paleosoils (Figs. 2a). It is overlain by the intrashelf external carbonate ramp deposits of the Sveti Duh fm., recording a regional transgressive event locally marked by a hard ground (Figs. 2b; Korbar et al., 2012) and providing a useful reference horizon for stratigraphic correlations. The Gornji Humac fm. mainly consists of rudist-bearing platform carbonates, with wackestone and packstone facies interlayered with rudist debris forming storm beds and tidal sandwaves (Figs. 2c). An erosional surface occurs at the top, with evidence for meteoric calcite cementation, karst dissolution and, locally, bauxite deposits (Fig. 2d; Kovačević Galović et al., 2012). This long-lasting erosional phase is testified by a regional stratigraphic gap spanning from Coniacian-Santonian to Ypresian times (Jelaska et al., 1994; Korbar, 2009; Mitterpergher et al., 2019). Sedimentation resumed in the Lutetian and Bartonian with the deposition of the ramp-carbonates regionally known as foraminiferal limestones (Fig. 2e), passing upward to the transitional beds (*Globigerina* marls) (Fig. 2f) and the predominantly shallow marine clastic succession of the Dalmatian flysch (Fig. 2g; Persico et al., 2019). The Eocene-Oligocene Velebit breccia outcrop just NW of the Paški zaljev and unconformably cover the folded cretaceous substrate (Fig. 2h). The youngest sediments exposed in the Pag Island are early Miocene freshwater lacustrine deposits, which unconformably lay on the folded and peneplanated substrate, and dip less than 20° to the north, testifying for mild deformation in the area since Miocene times (Fig. 2i; Bulić & Jurišić-Polšak, 2009).

4.2 Along-strike fold geometry

In map view, one of the most peculiar features of the Pag anticline and of the adjacent folds in the surroundings of Poveljana (Poveljana anticline from here onwards) is that they are dissected by two sets of subvertical strike-slip fault zones striking E-W and N-S (Fig. 3). The E-W striking set is dominant in the NW part of the Pag anticline, while the N-S set is better developed in the SE region and in the Poveljana anticline. The boundary between these two structural domains is marked by a couple of E-W subvertical fault zones compartmentalizing the fold into two structural domains with average fold axes showing 20° of strike difference. The northwestward domain is rotated clockwise compared to the southeastern domain in map view. In the north-western sector of the fold, the axis plunges gently towards $N318^\circ$, in the southwestern sector it is horizontal and trends $N123^\circ$ (Fig. 3).

The Pag anticline geometry is described in detail based on six NE-SW cross-sections shown in Figures 3a to 3f. The northern fold periclinal sector (Fig. 3a) consists of a triangle zone composed

of a gently southwest-dipping backthrust, that can be traced for about 3.5 km along strike, superposing the north dipping beds of the Gornji Humac fm. on the transitional beds and a forethrust juxtaposing the foraminiferal limestones on the transitional beds in the backlimb (**Fig. 6b**). The backthrust is segmented by east-west dextral transpressive faults and involves increasingly deeper structural levels moving towards the south (**Fig. 3b**). In section B, the backthrust juxtaposes the anticline crest on a vertical to overturned backlimb, both consisting of limestones of the Gornji Humac fm. The backthrust produces its maximum displacement around section B, while to the south it dies out through a series of low-displacement conjugate thrust planes, well exposed in the surroundings of section C (**Fig. 3c**). The combined effect of the backthrusts and of the dextral strike-slip faults is a clockwise rotation of the anticline crest above the backlimb, causing the observed variation in the trend of the anticline axis in the northern sector of the fold (**Fig. 3**). From north to south (from sections A to F), the forelimb increases its dip angle from 35–40° to 50–70°. The backlimb, visible only in sections B and C, passes from being vertical to overturned in section B to dipping at about 70° in section C, where a backlimb syncline crops out. Accommodation structures at the decameter to hectometer scale such as top-to-the-hinge duplexes, conjugated thrusts in the hinge zone and out-of-the-syncline thrusts (Price & Cosgrove, 1990; Mitra, 2002) are widespread around section C (**Fig. 3c**).

Along section D the anticline profile is nearly symmetrical, with forelimb and backlimb dipping at about 60–70°, and no major thrusts cropping out. The anticline nucleus is exposed in this sector and consists of well bedded Milna fm. limestones tightly shortened into a hectometric triangle zone (**Fig. 3d**). The Milna fm. is well exposed in the crestal area and is characterized by pluri-hectometric, asymmetric to symmetric parasitic folds and subsidiary thrusts and backthrusts, typically localized in finely layered stromatolitic beds and paleosoils. Section D intersects one of the sinistral strike-slip faults dissecting the anticline forelimb and compartmentalizing the fold.

Along sections E and F (**Fig. 3e**), the profile of the Pag anticline becomes asymmetrical again, with a vertical to overturned forelimb, a gently dipping backlimb and an open backlimb syncline. The forelimb is locally crosscut by splays of shallowly dipping secondary forethrusts, supporting the existence of a buried forethrust in this sector, as interpreted in the cross sections. Toward the foreland, a train of minor anticlines (Povljana anticline) exposing the Gornji Humac fm. in their nucleus is exposed. These anticlines are mostly symmetrical, except for the westernmost fold, where only the backlimb is visible. The anticlines have a box profile, with steeply dipping limbs and flat or gently undulating crestal area. Section F (**Fig. 3f**) intersects one of the N-S striking dextral strike-slip faults dissecting the anticline forelimb in this sector compartmentalizing and tearing different domains along strike (**Fig. 3f**). Moving towards the south, the interference between strike-slip faults and subsidiary thrusting is more complex and increases towards the southeast of Pag island producing rotated and dislocated blocks in the anticline crest. These dextral N-S strike-slip faults crosscut also the backlimb of the subsidiary forelandward anticline to the SW of the Pag anticline (**Fig. 3**).

5. STRUCTURAL DATA ANALYSIS

5.1 Deformation structures far from fault zones

Veins, joints and stylolites measured far from fault zones are referred to as background deformation structures. To simplify description and relative comparisons, data from adjacent

stations were grouped in 15 field sites and are illustrated both unrotated and rotated to restore bedding to the horizontal (**Fig. 4**). Information on station grouping into sites are provided in the supplementary material table **S1**.

Bed-parallel stylolites are abundant both in Cretaceous carbonates and in foraminiferal limestones (**Fig. 5a**). Mesostructures in the Cretaceous limestones include bed-parallel veins, few centimeters long, developed in re-opened bed-parallel stylolites, occurring both in the anticlinal crest and in the crest-limb transition zones. These veins are cross-cut by bed-perpendicular, longitudinal (axial-parallel) tectonic stylolites associated with transverse (axial orthogonal) calcite veins that commonly postdate stylolites (**Fig. 5b**). Longitudinal stylolites are locally reopened and filled by calcite cement. Transversal veins commonly abut facies boundaries or bioclastic levels in storm beds. The orientation of bed-perpendicular deformation structures depends on the position along the anticline axis, and it is influenced by the non-cylindrical fold shape in the pericline area, and by strike-slip related block rotations about vertical axes. Indeed, mean strike of longitudinal stylolites is N140°E in the northwestern sector and N120°E in the southeastern one, whereas the corresponding transverse veins strike is N50°E and N30°E, respectively, testifying for fold compartmentalization in a NW and a SE sector, separated by a major E-W left-lateral fault that produced postfolding block rotations (**Fig. 4**). The Gornji Humac fm. shows a different background deformation pattern in the northwestern pericline since bed-parallel and cross-fold veins do not occur here. Moreover, axial parallel stylolites are preceded by E-W striking stylolites (N100°), orthogonal to bedding, which locally show slickolites indicating left-lateral reactivation.

The oldest deformation structures in the foraminiferal limestones are rare NE-SW striking, transverse pressure solution cleavages, preferentially found in the forelimb. Apart from this local complexity, foraminiferal limestones are mainly affected by bed-perpendicular, longitudinal pressure solution cleavage striking NW-SE, associated with sub-vertical transverse veins striking NE-SW, a pattern like that found in Cretaceous limestones (**Figs. 4, 5c**). In the overlying Dalmatian flysch, thin longitudinal compaction bands occur, striking sub-parallel to the axis of the fold. They are crosscut by transverse joints, veins and by conjugate joints with acute angle bisector (60°) striking from N50° to 70°E (**Fig. 5d**). The latter are particularly abundant in well cemented globular concretions within sandstone strata.

The strike of subvertical cross-fold veins vary from NNE-SSW to ENE-WSW. The factors controlling the local orientation of cross-fold veins include: (i) block rotation due to late-stage strike-slip faults; and (ii) the veins locally forming as hybrid extensional and shear veins arranged in right-lateral NNE-SSW and left-lateral ENE-WSW *en échelon* arrays (e.g., Site 5; **Fig. 5e**). After back-rotating bedding to horizontal, right-lateral arrays strike N0°-10° (**Fig. 5f**) and left-lateral shear vein arrays strike N70°-80° (**Fig. 5g**). The formers are composed of N10° striking vertical veins associated with N100° striking vertical stylolites, partially re-opened and calcite cemented. The *en échelon* bed orthogonal shear vein arrays are deformation structures that accommodate local strike-slip and tearing deformation along the strike of the fold and occur also in other areas far from large thrusting related structures (N10°-30° veins in Site 12 in **Fig. 4**).

Meter-scale conjugated thrusts oriented at low angle to bedding have been observed in several outcrops of the Gornji Humac fm. in the backlimb of the Pag anticline. These thrusts appear to be passively rotated together with the fold limb (see *Chapter 5.2*). Upon bed restoration to horizontal, secondary thrusts are coherent with NW-SE contraction.

5.2 Fold accommodation faults

Reverse faults outcropping in the Pag anticline accommodate displacements on the order of meters to hectometres (**Figs. 3a-b-c**). Well-developed discrete thrusts with hectometre-scale displacements are present in the northern backlimb of the Pag anticline, while accommodation structures such as minor thrusts and arrays of duplexes are widespread, especially in the backlimb and within the anticlinal core.

The foreland-vergent thrust and the backthrust forming the triangle zone in section A (**Fig. 3a**) consist of sharp fault surfaces bounding imbricated duplexes (**Fig. 6a**). Thrusts dip at low to medium angle and determine significant bed rotations in their footwalls, where bedding is vertical to overturned (**Figs. 6b-c**). The foreland-vergent thrust juxtaposes the foraminiferal limestone onto the transitional beds, which are squeezed in a tight footwall syncline showing accommodation structures such as subvertical out-of-the-syncline thrusts (**Fig. 6a**). Subvertical bedding surfaces of transitional beds are exploited by late strike-slip faults. In a well exposed section of the main backthrust involving the Gornji Humac fm. and foraminiferal limestones, it is possible to appreciate its complex geometry consisting of multiple low angle slip surfaces, in turn composed of smaller scale anastomosing slip surfaces (**Fig. 6c**). Slip surfaces are locally decorated by calcite slickenfibers indicating top to the north-east movement. The vertical to overturned backlimb is crosscut by a splay of minor thrust branches and develops kink bands with gently dipping axial planes ahead of blind thrusts (**Fig. 6c**). The footwall of the backthrust, involving the Gornji Humac fm. and the foraminiferal limestones, shows axial parallel stylolites and bedding-parallel veins in verticalized beds, characterized by asymmetrical kink folds. The thrust fault core is composed of a half-meter thick coarse red fault breccia with interposed narrow cataclastic surfaces and abundant pressure solution. The shear fabric is composed of well-developed S-C structures. In the surroundings of thrusts crosscutting the Gornji Humac fm., fault-parallel to low angle *en échelon* arrays of thin veins occur. Crosscutting relationships indicate that thrust related veins cross-cut bed-parallel veins with an angle of about 15°-20° (**Figs. 6d**). Thrust related veins are, in most cases, crosscut by cross-fold veins. Arrays of medium to high angle dipping (40°-70°) thrust related tectonic stylolites, bordering lens shaped domains, frequently occur adjacent to thrust surfaces defining S-C deformation zones.

Other frequent accommodation structures in the backlimb of the Pag anticline include limb wedge thrusts (Price & Cosgrove, 1990; Mitra, 2002) and duplex arrays, both showing top to the hinge kinematics (**Fig. 7**). Wedge thrusts appear as high-angle, sharp faults bearing a meter-scale cataclastic layer and calcite slickenfibers on the slip surface (**Fig. 7b**). In other fold sectors, more complex thrust structures such as duplex arrays bounded by roof and floor thrusts develop. There, N40°-N50° dipping thrust fault zones with top to N220°-N230° kinematics (dip-slip) separate a vein rich hanging wall from a foliated cataclastic footwall. Main wedge thrusts are characterized by ramp-flat geometry where highly deformed shear lenses and duplexes form meter-thick deformation zones where bedding is sheared and bent, indicating top to the hinge shear. Verticalized thrust faults show strike-slip to slightly oblique transpressional kinematics, subparallel to the fold axis direction. The duplex imbrication and S-C foliation consisting of stylolites and calcite slickenfibers on the shear surfaces, indicate top to the hinge sense of transport (**Fig. 7c**). Isolated thrusts and conjugated thrusts are found also in sectors of the backlimb apparently less deformed (**Fig. 7d**). Such thrusts

accommodate displacements on the order of few centimeters, dip at high angle and have an angle of less than 30° with bedding (**Fig. 7d**). This evidence suggests that they formed and activated before folding and were then passively rotated during limb rotation.

The transition between backlimb and the gently dipping anticlinal crest occurs relatively sharply, and, where visible in cross-sectional exposures, it is marked by a stack of duplexes variably indented forming multiple fish-tail structures (**Fig. 7e**). Thrusts bounding the duplexes dip to the SW in the crest, and to the NE in the backlimb, suggesting a transport towards the hinge from both sides.

The anticlinal core is intensely deformed by multiple subsidiary thrusts and indentation structures. The deformation pattern associated with thrust fault zones in the Milna fm. shows high heterogeneity and complexity, due to the frequent occurrence of detachment horizons consisting of paleosoils and biogenic laminites. Towards the fold nucleus, duplexing is accommodated at a larger scale by passive roof thrusting and, at a smaller scale, by ramp thrusting, polyharmonic folding, and rarely by bed parallel slip (**Fig. 7f**).

The forelimb of the Pag anticline appears more regular than the backlimb, although parasitic folds and small-scale thrusts and duplexes are locally visible and could have been overseen because of the lack of cross-fold exposures. However, no evidence for map-scale reverse faults or thrusts have been found in the field.

5.3 Deformation pattern along pre-folding fault zones

Few fault zones are crosscutting the Gornji Humac fm. in the southeastern part of the Pag anticline forelimb showing a distinct deformation pattern characterized by soft-sediment deformation. Fault zone segments in Cretaceous limestones strike NW-SE to NNW-SSE and are characterized by foliated domains subparallel to the fault surface and surrounded by intensely fractured, fault-bounded and rotated, limestone beds (**Figs. 8a-b-c**). Fault subparallel foliation surfaces locally bear pockets of breccias with a micritic matrix. Kinematics along the NW-SE fault planes can be inferred from fault planes and pressure-solution cleavage intersection relationships indicating top to the SW sense of transport (**Figs. 8d-e**). Well-developed, systematic fracture patterns are not recognizable along these fault zones. The NW-SE fault zones dislocate the Cretaceous limestones only, showing ramp cutoff angles decreasing towards the older strata. Upon restoration of Gornji Humac fm. bedding to horizontal, the faults result dip at medium angle to the SW, with normal-oblique sense of movement. N-S strike-slip fault segments dislocating the foraminiferal limestones and the Dalmatian flysch join to, and partially reactivate, NW-SE fault segments. Dextral strike-slip reactivations are localized in fault segments with higher cutoff angles only (**Figs. 8d-e**). In the reactivated fault segments, brittle deformation structures overprint ductile, soft-sediment structures.

5.4 Deformation structures along strike-slip fault zones

Strike-slip fault zones are widespread, especially in the southern and northern sectors of the Pag anticline, and in the south-eastern part of the Poveljana anticline. In the central part of the Pag anticline, faulting is less intense (**Fig. 3**). Closely spaced strike-slip fault zones, each associated with several minor faults and their respective damage zones, causes the pervasive occurrence of fault-related veins in most of the study area. Fault-related veins are clearly recognizable from the

cross-fold veins because they strike oblique to the folded bedding and maintain vertical attitude irrespective of bed attitude.

Strike-slip faults accommodating right-lateral offsets strike N-S, whereas those with left-lateral offsets strike roughly E-W. The latter are concentrated in northwestern sectors of the anticline, while the former mainly developed in the southeastern part. NE-SW striking faults are locally developed and are more frequent in the central and northern sectors of the fold. They produce moderate offset, both dextral and sinistral. Many fault zones are localized along the limbs and crest-limb transition zones, producing maximum offsets of up to about 300 m that typically decrease towards the fold crest area. This feature causes along-strike compartmentalization of the forelimb into variably rotated fault-bounded blocks.

Both N-S and E-W fault sets trend obliquely with respect to the fold strike and their acute intersection angle varies between 80° and 90° (**Fig. 9a**). Strike-slip E-W and N-S fault damage zones in Cretaceous carbonates involve arrays of subsidiary splay faults trending sub-parallel to the master faults. Vertical to subvertical calcite veins are abundant and strike typically oblique (35° - 45°) and parallel to the main slip surfaces (**Figs. 9a-b**). Calcite cement fills both vein sets, has brownish to reddish color, and is extremely abundant in fault cores and damage zones of both strike-slip fault sets. Vertical, strike-slip fault-related tectonic stylolites are also abundant but show a higher spatial heterogeneity in the anticline compared to the veins. Sub-orthogonal vein and stylolite sets mutually crosscut (**Figs. 9c-d**). Locally, within E-W strike-slip fault damage zones, NE-SW veins associated with NW-SE stylolites, indicating left-lateral kinematics, are mutually cross-cut by deformation patterns indicating right-lateral reactivations (**Figs. 9a**). N-S right-lateral fault zones are characterized by fault-parallel veins whereas fault-parallel stylolites are rare and locally occur in the forelimb and in the NW pericline (**Fig. 9d**). Moreover, few N-S fault zones show dip-slip normal slickenlines and extensional offset.

The strike-slip fault pattern recognized in foraminiferal limestones along the forelimb of the Pag anticline is characterized by the formation of meter-wide domains of rhombohedral lithons bounded by pressure-solution seams and shear surfaces, in a S-C arrangement, associated with oblique calcite veins. In the overlying Dalmatian flysch, subsidiary E-W left-lateral and NE-SW right-lateral strike-slip fault zones occur (**Fig. 9a**), associated with *en échelon* vein arrays and foliated S-C domains (**Fig. 9e**). Near vertical ESE-WNW to E-W left-lateral strike-slip faults also affect late Miocene lacustrine sediments.

6. DIAGENETIC CEMENTS AND MICROSTRUCTURES

6.1 Petrography of host rocks and cements

The Milna fm. lagoonal limestones (Korbar, 2009; Korbar et al., 2012) contain pseudoprimary, planar-E to porphyrotopic dolomites formed in the peritidal depositional environment (**Fig. 10a**) that were later calcitized to produce micritic and microsparitic calcite cement with dolomite habit. Host rock limestone matrix show dull red luminescence in CL (HR_{Milna}; **Fig. 10b**). The Sveti Duh fm. mudstones and wackestones (HR_{S.D.}; Davey and Jenkyns, 1999; Korbar et al., 2012) show homogeneous orange matrix luminescence in CL. The grainstones, packstones and subordinate wackestones of the G.H. fm. (HR_{G.H.}; see **Figs. 10m-n**; Korbar et al., 2012; Brlek and Glumac, 2014) display dull purple color in CL.

Intergranular cement is composed of granular mosaic calcite while rare fenestrae and moulds are occluded by drusy calcite cement. Both cements show intense Type I twinning and are non-luminescent in CL. Paleosoils (HR_{topK}) and cements (C_{topK}) at the top of the G.H. fm., related to the K-T unconformity, show non-luminescence in CL. Cements are hosted in up to meter thick bed-parallel karst dissolution pockets, from which they grow inward with layered columnar habit (**Fig. 10c**). Foraminiferal limestone host rocks ($HR_{F.L.}$) are composed by two main facies types, wackestones and nummulitic grainstones, that show a dull purple and orange luminescence, respectively. Other types of calcite cements occur, namely $C_{D.F.}$ (**Figs. 10e-f**) and C_{late} (**Fig. 10d**), that fill intergranular porosity in the Dalmatian flysch and clog fractures related to late exposure (telogenetic), respectively.

Calcite cements in tectonic veins have been subdivided into four groups (V_1 , V_2 , V_3 and V_T) based on their petrographic characters, as detailed below. V_1 cement is found exclusively in bed-parallel veins. V_1 calcite crystals are “milky white”, show a blocky structure, include pervasive Type I twinning (Burkhard, 1993), and are non-luminescent in CL (**Fig. 10c-d**). V_T calcite cement is hosted in thrust related veins and is characterized by non-equigranular habit, non-luminescent in CL with intense Type I twinning (**Fig. 10e-f-g-h**). V_2 calcite fills crossfold veins and conjugate shear vein arrays orthogonal to bedding and are composed of a non-equigranular mosaic calcite, non-luminescent in CL and with rare Type I twinning, less intense than in V_1 and V_T calcites (**Fig. 10c-d-e-f-i-j**). In proximity of the unconformity at the top of the Gornji Humac fm., V_2 calcite cement has dull orange color in CL (**Fig. 10c-d-i-j**) while vein rims show solid inclusions zones with dolomitic habit that emit a purplish color in CL. Fracture-filling dolomites are recognizable by their inclusion zones habit even in transmitted light only and are planar-E (**Fig. 10c-d-i-j**). Cross-fold V_2 veins in foraminiferal limestone host blocky, dogtooth, fibrous and microsparitic calcite cements ($V_{2F.L.}$), characterized by different Type I twinning intensities. They share the same CL color with their encasing host rocks, therefore, $V_{2F.L.}$ calcite veins in wackestones show dull red to purple colors, while those that cut through nummulitic grainstones are orange (**Fig. 10k-l-m-n**). V_3 calcite cement shows non-luminescent, yellow, and bright orange growth zones in CL (**Fig. 10b-h-j-n**). Type I twinning locally occurs. Where V_3 precipitated along re-opened and cemented axial parallel stylolites, calcite crystals show smaller dimensions, rounded habit and a marked yellowish to reddish halo in transmitted light. Along strike-slip fault zones, $V_{2F.L.}$ are re-opened by $V_{3F.L.}$ calcite cement (**Fig. 10m-n**), similarly to V_2 and V_3 in Cretaceous formations (**Fig. 10i-j**). The Dalmatian flysch host transversal veins which are composed of calcite cement with rare Type I twinning and show the same orange color in CL as the intergranular calcite cement ($C_{D.F.}$). Finally, brownish, banded karst-related calcite cements (C_{late}), tenths of centimeters thick, occur in late extensional pockets, mainly along N-S and E-W strike-slip zones, independently of stratigraphy, and show non-luminescence in CL.

6.2 Carbon and oxygen isotope ratios of host rocks and cements

Results of carbon and oxygen stable isotopes analyses are illustrated in **Figure 11a** and in **Table 1**. Mean and standard deviation values of the results are shown in **Figure 11b** along with the diagenetic fluid types. The legend above the results illustrates cements in a relative time framework and relates them to the fluid types and the tectonostratigraphic context. The green dashed squared area indicates the range of $\delta^{18}O_{\text{‰}}$ and $\delta^{13}C_{\text{‰}}$ (V-PDB) values of limestones precipitated in equilibrium with Late Cenomanian to Early Coniacian seawater (**Fig. 11a**; Veizer et al., 1999).

Eocene seawater $\delta^{18}\text{O}$ and $\delta^{13}\text{C}$ values are not shown in the plot: they are comprised between -1‰ to +0.5‰ and +0.8‰ to +3.6‰, respectively. $\delta^{18}\text{O}$ values of Cretaceous limestone host rocks show a similar range comprised between -6‰ and -3.5‰. Their $\delta^{13}\text{C}$ values show slightly different ranges, comprised between 0‰ and +3‰. Host rocks and cements, at the top of the Gornji Humac fm., have $\delta^{18}\text{O}$ values in the range of Cretaceous host rocks but $\delta^{13}\text{C}$ values are highly depleted compared to host rocks and range from -10‰ to -2‰. The foraminiferal limestone host rocks show the most enriched $\delta^{18}\text{O}$ values, from -4.5‰ to -2.5‰, and $\delta^{13}\text{C}$ values comparable to the Cretaceous limestones. V_1 and V_T calcite cements have $\delta^{18}\text{O}$ values 1‰ depleted compared to the Cretaceous limestones but similar $\delta^{13}\text{C}$ values. V_2 calcite cement has the most depleted $\delta^{18}\text{O}$ values, ranging -9‰ to -6‰ and $\delta^{13}\text{C}$ from -4‰ to +2‰. $V_{2\text{F.L.}}$ calcite have $\delta^{18}\text{O}$ and $\delta^{13}\text{C}$ values comparable to V_1 and V_T . The Dalmatian flysch hosts intergranular calcite cement filling also transversal veins, $C_{\text{D.F.}}$, that shows $\delta^{18}\text{O}$ values ranging from -5‰ to -3‰ and $\delta^{13}\text{C}$ values around 0‰. V_3 and $V_{3\text{F.L.}}$ calcite cements have a $\delta^{18}\text{O}$ range of -6.5‰ to -4.5‰ and $\delta^{13}\text{C}$ values of -7‰ to -1‰, like HR_{topK} and C_{topK} . Fault cores of strike-slip faults show lower $\delta^{18}\text{O}$ and $\delta^{13}\text{C}$ values compared to the undeformed host rocks, from -6‰ to -3‰. Late calcite cements (C_{late}) along strike-slip faults show $\delta^{18}\text{O}$ values comparable to HR_{topK} , C_{topK} , V_3 and $V_{3\text{F.L.}}$ and depleted $\delta^{13}\text{C}$ values, from -11‰ to -7‰.

7. DISCUSSION

7.1 *Relative chronology of deformation structures and progressive fold evolution*

Here, we first reconstruct the evolution of deformation structures in the Pag anticline based on the combination of field structural data and the petrography of vein cements (**Fig. 12a**) for both background (**Fig. 12b**) and fault-related deformation patterns (**Fig. 12c**). According to our results, the oldest structures are soft-sediment normal faults which affected the Cretaceous limestones just after deposition of the Gornji Humac fm. Their orientation after bed restoration to the horizontal is oriented almost parallel to the present-day NW-SE dominant structural trend in the area. These extensional structures could be related to destabilization of the carbonate platform environment and to foreland flexuring during the forebulge stage of Adria, which was likely to be subparallel to the thrust and fold belt (Tavani et al., 2015; Tavani et al., 2018; Beaudoin et al., 2022). Then, Cretaceous formations were exposed to long-lasting subaerial conditions and erosion although other fracture systems and deformation structures related to this stage were not identified in the Pag anticline (Mittempergher et al., 2019).

Deposition of the foraminiferal limestones marked the onset of the foreland basin stage in the region, in Ypresian times (Piccoli and Proto Decima, 1969; Babić et al., 1993; Pamić et al., 1998; Persico et al., 2019). In the foreland basin stage, the burial of Cretaceous limestones reached at least 600 m (Sokač et al., 1976) due to the deposition of the Lutetian-Bartonian Dalmatian flysch, providing the necessary sedimentary load for development of bedding-parallel stylolites, that formed in the studied Upper Cretaceous carbonate succession (**Fig. 12b**).

Folded bed parallel veins in Cretaceous limestones, locally reopening burial stylolites and associated with longitudinal tectonic stylolites perpendicular to bedding (**Fig. 12b**), indicate a pre-folding Andersonian compressive stress field with a vertical minimum principal axis of the stress ellipsoid σ_3 (**Fig. 13a**). Longitudinal tectonic stylolites orthogonal to bedding occur both in the Cretaceous and in the foraminiferal limestones. Folded, bed-perpendicular longitudinal compaction bands in the Dalmatian flysch indicate that the pre-folding contraction in synorogenic strata

occurred in soft sediment conditions. Overall, the pre-folding synorogenic background deformation pattern indicates a maximum principal axis of the stress ellipsoid σ_1 oriented perpendicularly to the fold axial trend, mainly from N40° to N50°. This deformation pattern was likely produced during the layer parallel shortening stage.

Folded deformation patterns include conjugate thrust pairs, thrust-related veins cemented by V_T calcite at low angle to bedding, and stylolites oblique to bedding that mostly strike N130° to N140°, i.e., parallel to thrusts. Bed restoration to the horizontal allows to reconstruct an Andersonian compressive stress field with vertical σ_3 and NE-SW (N40° to N50°) striking σ_1 (i.e., in very good agreement with that inferred from pre-folding bed-perpendicular stylolites (**Fig. 13a**)). Conjugate thrusts likely formed when layer-parallel shortening transitioned to multilayer folding. Local shear failure led to localization of compression in conjugate thrusts and other minor structures, which were then involved in folding. This generally occurs in thick competent units (Ramsay, 1981; Price and Cosgrove, 1990; Morley, 1994; Mazzoli et al., 2022). In the northwestward pericline of the Pag anticline, older WNW-ESE striking, mesoscale thrust fault zones and associated contractional deformation structures are cross-cut by NW-SE striking thrusts, backthrusts and fold-accommodation structures. Many tectonic stylolites far from fault zones strike E-W in the pericline in the Gornji Humac fm. Additionally, in the northwestern sector of the forelimb, the oldest deformation structures in the foraminiferal limestones are NE-SW striking tectonic stylolites. These azimuthal variations may suggest local rotations of the compressive stress field trajectories, that could be related with the migration of the pericline in the early stages of buckle folding.

Formation of NE-SW striking cross-fold veins V_2 and V_{2FL} in Cretaceous limestones and foraminiferal limestones, respectively, and continuing nucleation of axial parallel tectonic stylolites as suggested by mutual crosscutting relationships (**Fig. 12**), indicate the switch between σ_2 and σ_3 stress axes, possibly triggered by the onset of folding and later by amplification of the Pag anticline (**Fig. 13b**; Marshak, 1988; Macedo & Marshak, 1999; Tavani et al., 2015). Increasing the vertical load by sedimentation of the proximal turbidites in a tectonically controlled basin may have favoured buckle folding of the multilayer and the switch from a contractional (vertical σ_3) to a strike-slip stress field configuration (vertical σ_2 ; Babić & Zupanič, 2008; Persico et al., 2019). The strike of V_2 veins indicates that the direction of σ_1 during the folding stage was still from N40°E to N50°E, while the direction of σ_3 was parallel to the axis of the Pag anticline, i.e., a strike-slip stress field configuration. The timing of folding is well constrained by the occurrence of the Promina alluvial deposits along strike of the Pag anticline towards the SE, which are represented by a late Eocene to early Oligocene synfolding shallow marine to alluvial succession, unconformably overlying the Dalmatian flysch (Mrinjek, 1993; Tari-Kovačić and Mrinjek, 1994; Babić and Zupanič, 2007). E-W stylolites that previously formed in the pericline, were reactivated by sinistral transpression, and NE-SW stylolites that formed in the forelimb were re-opened and filled by V_{2FL} calcite, as transversal veins (**Fig. 13b**).

Fold-related deformation structures consist mainly in accommodation structures concentrated in the hinge zones and in the backlimb. After significant bed rotation fold locking likely produced strain hardening. These structures eventually propagated into thrusts and backthrusts showing high cutoff angles in the fold limbs and into out of syncline thrusts (Ramsay, 1981; Price and Cosgrove, 1990; Morley, 1994; Mazzoli et al., 2022). Fold tightening was also characterized by strike-slip reactivation of previously formed prefolding and synfolding deformation structures, including conjugate strike-slip shear fracture arrays, and rotated thrust fault zones. Lastly, right- and left-

lateral strike-slip faults, with N-S and E-W azimuths respectively, favored differential limb tearing and rotation about vertical axes of fault-bounded blocks (**Figs 12c, 13c**; Fischer & Jackson, 1999; Mitra, 2002; Leticariu et al., 2005; Evans & Fischer, 2012).

The tectonic activity of N-S right-lateral and E-W left-lateral strike-slip fault zones continued in the late to post-folding stage, in an overall right-lateral transpressional tectonic regime (Korbar, 2009; Placer et al., 2010; Van Unen et al., 2019), as indicated by fault-parallel compression of E-W fault zones, recorded by fault-parallel stylolites, and dilation along N-S fault zones, recorded by pervasive N-S striking V_3 and V_{3FL} calcite veins. Longitudinal stylolites and transversal vein arrays were re-opened by V_3 cements, which also mineralized veins locally formed along thrust faults, documenting their strike-slip re-activation in the post-folding stage (**Fig. 13c**; Schmid et al., 2008; Van Unen et al., 2019). Onset of strike-slip fault-related deformation may be associated with the tectonic evolution that affected the Dinarides Orogen since the Oligocene, which caused the CCW rotation of stable Adria and the Adriatic islands by 20-25° respect to the European plate and facilitated fold tightening (Merlini et al., 2002; Márton et al., 2003; Ilić & Neubauer, 2005; Ustaszewski et al., 2008; Korbar, 2009; Márton et al., 2010, 2014; De Leeuw et al., 2012; Kastelić & Carafa, 2012). Additional rotation of the region from Miocene to present was less than 10° CCW (Le Breton et al., 2017). In the Pag anticline, transpressional tectonics resulted in a strike-slip stress field with a N40° to N50° oriented σ_1 that led to localization of dextral shearing along N-S to NNE-SSW strike-slip faults and right-lateral shearing on E-W to ENE-WSW strike-slip faults (**Fig. 13c**).

Towards the northern periclinal termination of the Pag anticline, the fold axis trend is rotated by about 20° compared to the central sector, the fold crest is bounded by a backthrust and the fold profile is asymmetric and verges towards the hinterland (**Fig. 3**). The backthrust associated with the E-W trending left-lateral strike slip faults are kinematically coherent with a clockwise rotation of the whole northern fold sector (**Fig. 14**): the offset determined by the backthrust is maximum towards the northern pericline and fades towards the central sector of the fold. The observed rotation of the periclinal sector likely occurred in the late stages of fold propagation since it is associated with a backthrust clearly crosscutting the folded strata (**Fig. 6c**).

The observed clockwise rotation could be caused by an incipient oblique linkage (e.g., Nabavi & Fossen, 2021) of the Pag anticline with the periclinal termination of the overturned fold present to the NE (**Fig. 14**). A clockwise rotation is also coherent with the regionally inferred dextral transpression of the area (Korbar, 2009), although the relationships with the NEAF remain uncertain due to the lack of precise information about the NEAF location, orientation, and kinematics.

The southern sector of the Pag anticline shows higher structural complexity, and the periclinal termination is not visible; there the fold asymmetry is opposite than in the northern sector, a forethrust is locally emerging and the footwall syncline is tighter than in the central and northern sectors (**Fig. 3**). The opposite asymmetries of the fold profiles are generally coherent with a component of clockwise rotation of the whole fold, in a framework of dextral transpression. However, in the southern sector the activity of the N-S right lateral faults appears unrelated with the activation of the forethrust: they produce a shift of the fold axial plane to the south, and a counterclockwise rotation of the limb blocks in both the Pag and Poveljana anticlines, where bedding strikes nearly ESE-WNW.

7.2 Pag and Poveljana anticlines folding mechanism and detachment depth

The structural style in the study area is well illustrated by a cross-section cutting through the Pag and Poveljana anticlines, traced in the central sector of Pag Island (**Fig. 15**, section E in **Fig. 3**). Only the Poveljana anticline is entirely exposed and shows an almost symmetrical double pop-up with a “crestal syncline” separating two opposite-verging, subsidiary folds. Conversely, the Pag anticline in the southern structural sector has a markedly asymmetrical shape, verging to the SW, and is affected by limited thrust breakthrough at the transition between the forelimb and the adjacent outer syncline. Overall, field data can be interpolated by a train of folds associated with subsidiary fold accommodation faults, a structural style which can be interpreted as due to buckling (e.g., [Price and Cosgrove, 1990](#); [Butler et al., 2020](#)). We applied the excess area construction ([Epard and Groshong, 1993](#)) to geometrically constrain the depth of the supposed detachment level. Based on this construction, the detachment of the Pag anticline is estimated to lay between 2.5 to 2.9 km below sea level, i.e., in the Upper Jurassic Evaporite Complex (*sensu* [Tari-Kovačić and Mrinjek, 1994](#)), identified in wells located a few tens of km southeast of the Pag anticline (RK, Ravni Kotari; see **Fig. 1c**). The detachment depth calculated for the Poveljana anticline results to be 1 km deeper, at 3.9 km depth. The difference in the depth to detachment compared with the Pag fold can be explained due the composite fold shape that lowers the gradient of the regression line or simply due to random fold nucleation pattern in the multilayer ([Price and Cosgrove, 1990](#)). The depth of the Pag anticline agrees with that proposed by [Đurasek et al. \(1981\)](#) and [Korbar \(2009\)](#) for the basal detachment of the Ravni Kotari-northern Dalmatia tectonic unit. However, since the incompetent unit underlying the competent mechanical control unit has no thickness constraints, the calculated detachment depth represents a minimum value. Results of the excess area analysis indicate that the fold train in the cross-section accommodated a horizontal shortening of about 16%.

The geometrical characteristics of the Pag and Poveljana anticlines are here discussed to interpret the mechanical behavior of the folded carbonate multilayer in the area, consisting of at least 1.65 km of layered platform carbonates (**Fig. 15a**). The Pag anticline and the northern sector of the Poveljana anticline have a considerable hinge line length, up to 40 km based on the geological map of Croatia ([Mamužić & Sokač, 1973](#); [Sokač et al., 1976](#)). Long anticlines with fully connected hinge lines generally result from in-phase buckle folding ([Ramsay, 1981](#); [Price and Cosgrove, 1990](#); [Butler et al., 2020](#)). It is shown by analogue models that buckling becomes self-organized (in-phase) with a dominant wavelength which depends on layer thickness after 35% shortening ([Dubbey and Cobbold, 1977](#)), which is much more than the shortening observed in the Pag – Poveljana area (16%). Accordingly, the wavelength of the northern Dalmatian fold train is ~4-5 km but is not systematic and shows local heterogeneities, like in the Poveljana anticlines (~3 km). The length and regularity of the fold hinges in the area cannot thus be ascribed to in-phase buckling of a unique mechanical layer encompassing the Jurassic and Cretaceous platform carbonates. Another evidence suggesting that the carbonate sequence did not behave as a single mechanical layer comes from the analysis of the slenderness ratio, i.e., the ratio between the fold wavelength and the thickness of the control unit. The slenderness ratio lays between 2.4 and 3, too low to induce buckling in a single layer, which requires a minimum value of 4 ([Ramsay, 1981](#); [Price & Cosgrove, 1990](#)). This implies that the Cretaceous limestones in northern Dalmatia can not be considered as a single mechanical unit but behaved as a complex multilayer sequence containing different control units ([Ramsay, 1981](#); [Price and Cosgrove, 1990](#); [Butler et al., 2020](#)). Buckling preferentially occurs in layered, anisotropic sequences rather than in an isotropic unit with equivalent thickness ([Ramsay,](#)

1981; Price and Cosgrove, 1990), and at burial depths lower than the dominant wavelength. The buckling process is, in fact, favored at shallow crustal depths because the critical buckling envelope is intersected before the shear fracture envelope (Jamison, 1987). The variable mechanical properties of the carbonate multilayers cropping out in the Pag anticline, including bed thicknesses and strength of the bed interfaces, caused the formation of polyharmonic and parasitic folds, i.e. folds having a shorter wavelength in the Milna fm., in the fold nucleus, which is characterized by thin limestone strata separated by weak interfaces consisting of oxides-rich paleosoils and microbial laminites (Fig. 7f; Ramsay, 1981; Price and Cosgrove, 1990).

Fold amplification in multilayers deformed by buckling produces box-fold geometries, with oblique axial planes and regular fold spacing (Blay et al., 1977; Price and Cosgrove, 1990), characters which are well represented in the uppermost structural levels of the Pag and Poveljana anticlines. Conjugate box-folds, as the Pag anticline, develop in mechanical multilayers characterized by well-spaced stiff layers with different thicknesses, and limited flexural slip due to the relatively high frictional strength of bed interfaces. In the Pag anticline, flexural slip is mostly localized in the hinge zones between the backlimb and the crest, and between the crest and the forelimb. Layer thickness is constant throughout the fold profile, characterized by convergent cleavage (i.e., fold type 1B; Ramsay, 1967). This strain distribution is typical of multilayers deformed by tangential longitudinal strain and with low mechanical anisotropy (Biot, 1965; Honea and Johnson, 1976). The occurrence of a series of accommodation structures such as a major backthrust, out-of-syncline thrusts, fish-tail duplexes in the backlimb, however, documents significant flexural slip folding compared to the forelimb. This asymmetrical strain distribution might come from the interaction of the backlimb with the front of the Velebit mountains (Fig. 1) located immediately behind the Pag anticline. The localization of flexural slip, flexural flow and accommodation structures close to the hinges indicates that fold amplification occurred mainly by limb rotation, after brittle failure along the hinges (Ramsay, 1981; Price and Cosgrove, 1990).

7.3 Paleostress during the evolution of the Pag anticline

We inverted fault slip, tectonic veins and stylolites data after separating them according to their deformation stage to reconstruct the paleostress during the tectonic evolution of the Pag anticline (Figs. 16a, b). Unfortunately, faults with slickenline data are scarce, but compensated by the amount of veins and stylolites data. Results of different structural sites, illustrated in Table 2, are quite inconsistent between each other and not robust. Nonetheless, they show a NE-SW oriented σ_1 in almost all the cases. Thrust-related deformation structures formed in a contractional stress field with vertical σ_3 , while both background deformation structures far from fault zones and those related to strike-slip fault zones formed in a strike-slip to transpressional stress field with vertical σ_2 (Figs. 16a, b). Our bootstrapping allows calculating the confidence contours for the principal axis orientations and the confidence interval for the stress tensor shape ratio R of the mean stress tensors by applying a random sampling with substitution scheme. Confidence intervals and shape factor ratios are shown in Table 2. The calculated mean stress tensor of the thrust-related deformation structures is characterized by a N50° directed σ_1 in a contractional stress field (Fig. 16c). The stress tensor calculated from background deformation structures indicate a N47° directed σ_1 in a transpressional stress field (Fig. 16d). The stress tensor calculated from the post-fold fault-related structures, similarly to the latter, is characterized by a transpressional stress field, and a N41°

oriented major stress axis direction (**Fig. 16e**). Coherent results from paleostress analysis in the pre-, syn- and post-folding evolutionary stages further confirms that all the studied mesoscale deformation structures in the Pag anticline developed in the main Dinaridic tectonic phase (*sensu* Blašković, 1998, 2005), mostly characterized by NE-dipping and SW-verging thrusts and related folds. Initially, the Dinaridic tectonic phase imprinted a contractional stress field in the study area that transitioned to a transpressional one during evolution of the Pag anticline. The post-fold fault-related stress field tensors show a higher dispersion compared with the other groups of tensors and include one site with an apparently extensional stress regime (site 4). The extensional tensor agrees with dip-slip normal lineations sporadically occurring on few N-S subvertical faults. Post-folding normal faulting has been documented also in paleostress reconstructions in other areas of the External Dinarides and interpreted as related with the deposition of the Miocene intramontane basins of the Dinaric Lake System (e.g., Ilić & Neubauer, 2005; Žibret & Vrabec 2016; Palenik et al., 2019; van Unen et al., 2019). The wide dispersion angle of σ_1 is likely due to the homogeneous orientation of subsidiary faults and veins around the main strike-slip faults, and the consequent inhomogeneous strain distribution. The most robust results are obtained in sites where fault planes orientations are more scattered (e.g., site 14).

7.4 Fluid sources and diagenetic environments of cements precipitation

Here, we discuss the possible interpretation of stable isotope data based on the main fluid sources likely to be involved in the tectonic evolution of the area, i.e., seawater and meteoric water, and their possible evolution due to the interactions with the wall rock. Light $\delta^{18}\text{O}$ values, like those of Cenomanian to Coniacian limestones in the Pag host rocks (**Fig. 11**), have been extensively documented in Cretaceous limestones of the Adriatic Carbonate Platform and have been interpreted as proof of limestone precipitation in coastal and lagoonal environments influenced by freshwater dilution (Vlahović et al., 2005; Tesović et al., 2011). Nevertheless, considering that the Gornji Humac fm. was eroded by a long lasting sub-aerial exposure, its $\delta^{18}\text{O}$ values could have been slightly modified by meteoric diagenesis (**Fig. 17a**). Paleosoils (HR_{topK}) and cements (C_{topK}) associated with the unconformity, at the top of the Gornji Humac fm., display strongly depleted $\delta^{13}\text{C}$ values. Their oxygen stable isotope ratios are comparable to the most depleted values of Cretaceous limestones host rocks supporting meteoric alteration of the Cretaceous platform during the forebulge stage. Their $\delta^{13}\text{C}$ values are as low as -10‰ and their mean value is comprised between -5‰ and -6‰, respectively, indicating that their carbon source is derived from microbial organisms and/or vegetation that colonized the Adriatic carbonate platform top during sub-aerial exposure (**Fig. 17a**; Vlahović et al., 2005; Korbar, 2009; Brlek & Glumac, 2014).

The foraminiferal limestone host rocks show $\delta^{18}\text{O}$ values comparable to other carbonates that deposited in early Eocene times, in the Neo-Tethyan realm. $\delta^{18}\text{O}$ values of limestone host rocks ranging from -2.5‰ to -4.5‰ can be the result of direct precipitation from seawater at water temperatures higher than 30 °C. The latter phenomenon occurred in surficial waters during the Early Eocene Climatic Optimum, which is contemporaneous to foraminiferal limestone deposition (**Fig. 17b**; Holail, 1994; Dinçer, 2016). Host rocks $\delta^{13}\text{C}$ values support this interpretation since they are in the range of Eocene marine waters (Veizer et al., 1999). Intergranular calcite cement, $\text{C}_{\text{D.F.}}$, that precipitated after nucleation of compaction bands induced by layer-parallel shortening (**Fig. 17b**) hosted in the Dalmatian flysch shows the heaviest $\delta^{18}\text{O}$ values amongst the studied cements. This could be both the result of a minor temperature effect, being the Dalmatian flysch the

shallowest studied unit, or due to null contributions of meteoric fluids during syntectonic precipitation.

Vein cements host only monophasic aqueous fluid inclusions indicating that their precipitation temperatures are reasonably below 50 °C. This is further corroborated by the shallow burial conditions experienced in the area and by the low geothermal gradients (see *Chapter 2*). V_1 and V_T vein calcite cements have $\delta^{18}\text{O}$ values slightly depleted compared to their host rocks, indicating that during layer-parallel shortening Cenomanian to Coniacian marine fluids, that constitute most of the volume of connate fluids (excluding the top of the Gornji Humac fm. interested by significant meteoric diagenesis), were slightly heated and precipitated at temperatures up to maximum 10 °C higher than seawater (**Fig. 17b**; O'Neil et al., 1969; Muchez et al., 1995; Hoefs, 1997). If this interpretation is correct, the lighter oxygen values are mainly the result of syntectonic precipitation temperatures higher than that of seawater during primary precipitation rather than other meteoric fluid inputs.

V_2 and $V_{2\text{F.L.}}$ vein calcite cements precipitated during the synfolding stage and are characterized by the most depleted $\delta^{18}\text{O}$ values. V_2 calcite has $\delta^{18}\text{O}$ mean values 3‰ lighter than Cretaceous host rocks values and, similarly, $V_{2\text{F.L.}}$ calcite is characterized by $\delta^{18}\text{O}$ values 2.5‰ lighter than foraminiferal limestones host rocks, indicating that fluids migrating during folding precipitated at temperatures of 50 and 45 °C if mostly connate and seawater-derived (assuming equilibrium precipitation), or that they were affected by a certain degree of mixing with meteoric fluids expelled by topography-driven flow of the already exposed fold and thrust belt (**Fig. 17c**; O'Neil et al., 1969; Friedman & O'Neil, 1977). $\delta^{13}\text{C}$ values in V_2 calcites show a decreasing trend approaching the top of the Gornji Humac fm. due to the Cretaceous to Paleocene meteoric/phreatic diagenetic inheritance. All the others $\delta^{13}\text{C}$ values of V_2 and $V_{2\text{F.L.}}$ calcites are in the range of carbonates precipitated from seawater (0‰ to +2‰). Therefore, we deduce from stable isotope ratios that the carbon source for calcite cements V_1 , V_T , V_2 and $V_{2\text{F.L.}}$ was locally provided by connate and seawater-derived fluids that equilibrated with the hosting limestone strata. Only few synfolding calcite cements show highly depleted $\delta^{18}\text{O}$ values indicating that meteoric fluids could have locally mixed at a higher degree with connate diagenetic fluids prior to calcite precipitation indicating very shallow burial conditions during the synfolding stage.

V_3 and $V_{3\text{F.L.}}$ vein cements are characterized by $\delta^{18}\text{O}$ and $\delta^{13}\text{C}$ values comparable to HR_{topK} and C_{topK} cements, indicating that meteoric fluids infiltrated and migrated along strike-slip faults, carrying in solution ^{12}C light carbon produced by organic matter at the surface, testifying for uplift and emersion of the Pag anticline during late to post-folding strike-slip deformation (**Fig. 17d**; Allan and Matthews, 1982; James and Choquette, 1990).

7.5 Coupling tectonics and paleofluid evolution

Fracture permeability is of primary importance in low-porosity carbonate rocks that were affected by intense cementation and primary porosity occlusion as in the case of the Pag anticline. Long-lasting subaerial exposure caused abundant eodiagenetic meteoric calcite precipitation which reduced intergranular porosity, drastically diminishing the matrix permeability of the carbonate rocks (James and Choquette, 1990). The Pag anticline structure developed by buckle folding of a

carbonate multilayer. Brittle deformation structures constituted most of the permeability network in these rocks, where abundant dissolution and cementation processes occurred.

During layer-parallel shortening, conjugate thrusting, and early buckle folding, the permeability was essentially controlled by bed parallel veins, longitudinal stylolites and by meter to decameter-scale conjugate thrusts and fish-tail structures (e.g., [Fischer & Jackson, 1999](#)). The short extent of these structures, combined with an essentially local origin of the fluids involved in vein cementation document a poor connectivity among mesoscale deformation structures. Bed-confined, layer-parallel veins, strongly buffered at the bedset-scale, likely caused decreasing permeability orthogonal to bedding, impeding vertical fluid migration after cementation. Layer-parallel shortening and the first stages of buckle folding therefore occurred in a closed, compartmentalized fluid system, possibly subject to rises in fluid pressure, which was relieved only locally by the opening of extensional fractures with limited length. Buckle folding of multilayers at shallow depth requires high fluid pressure to overcome the shear strength of bed contacts ([Ghosh, 1968](#); [Jamison, 1987](#)). Folding-related transversal fracturing and accommodation structures propagation progressively created the conditions for an efficient open, compartmentalized, 3D fracture permeability structure ([Beaudoin et al., 2022](#)), in which modified seawater fluids migrated laterally in the shallow burial environment, still influenced at the bedset-scale, by the preceding eodiagenetic meteoric inheritance, as documented by isotopic results. The fold tightening to post-folding activity of N-S and E-W strike-slip fault zones ensured hydraulic connectivity between fold limbs and produced effective conduits for vertical and lateral fluid flow during uplift ([Mucchez et al., 1995](#); [Leticariu et al., 2005](#); [Evans & Fischer, 2012](#)). Hydraulic connectivity likely allowed fluid pressure discharge and the build-up of higher differential stresses during the post-folding strike slip faulting, as testified by the abundance of fault related fracturing, shear failure and the widespread occurrence of cataclasites (e.g., [Cox, 2010](#)).

Overall, we infer that fluid migration pathways were compartmentalized (bedset to stratigraphic unit scale), from the layer parallel shortening stage up to the incipit of post-folding ([Roure et al., 2005](#); [Beaudoin et al., 2022](#); [Berio et al., 2022](#)). As soon as both inherited and newly formed fault zones increased their damage-related fracture network permeability during fold tightening, and subsequently, strike-slip faulting, the system opened and fluid mixing between adjacent reservoirs occurred. Moreover, when strike-slip faults eventually breached the surface, they acted as conduits for direct and abundant infiltration of meteoric fluids in the whole fracture network.

8. CONCLUSIONS

We performed a structural, petrographic, and isotopic study of the deformation structures and related cements exposed in the Pag anticline, in the External Dinarides of Croatia. Field and laboratory data have been integrated with geological mapping and cross-section reconstructions. The results of our work can be summarized in the following points:

1. The Pag anticline has a box fold geometry crosscut by high-angle to vertical left- and right-lateral strike-slip fault zones trending E-W and N-S, respectively. The fault sets make a wider angle than expected for transversal conjugate strike-slip fault pairs associated with folding.
2. Fold geometry suggests buckle folding of the multilayer as the main mechanism, dominated by flexural flow in the backlimb and by a higher degree of tangential longitudinal strain in the

This article is protected by copyright. All rights reserved.

forelimb. Depth-to-detachment calculation indicate that the Pag anticline could detach in the Upper Jurassic evaporitic complex, at minimum depths of 2500-2900 m. This is an example of shallow burial fold, whose amplification was likely to have been controlled mostly buckling and not by the propagation of an underlying fault of comparable size.

3. The geometry of the Pag anticline is strongly controlled by the interaction and overstepping of systems of thrust-backthrust faults. In the northern sector of the fold, backthrust activity produced northeastern facing and a steeply dipping to near vertical backlimb, whereas the forelimb dips more gently and has a very regular along strike geometry. Moving southward, the overlap area between backthrust-dominated and forethrust-dominated is characterized by a tighter fold geometry: the forelimb gradually becomes vertical to overturned and the backlimb maintains a high angle dip and is affected by a higher structural complexity with subsidiary thrust faults forming an articulated and anastomosed hectometric wide deformation zone in map view. Further to the south, fold asymmetry switches to a southwestward facing.
4. Paleostress analysis indicates that the evolution of the Pag anticline occurred in a stress field that transitioned from contractional to transpressional, maintaining a N40-50° oriented major stress axis during the main Dinaridic tectonic phase that occurred in late Eocene to early Oligocene.
5. Evidence from structural diagenesis supports the evolution from a bedset confined fluid system to a cross-formational one only during late-stage fold tightening. Such a switch in the fluid circulation was favored by the development of strike-slip faults dissecting the anticline. This implies that particular attention should be paid in reservoir structural characterization to the presence of late-stage, low-displacement strike-slip faults because of their role of effective conduits for vertical fluid flow. Moreover, we remark the role of inherited eodiagenetic fluids for influencing later cement isotopic patterns and changing the mechanical properties of the rocks. Specifically, eodiagenesis produces a stiff, irregular, mechanical unit with low porosity that could act as a mechanical flaw of the multilayer.
6. This work indicates that, despite some additional complexity, a quite classical fold-related fracture deformation pattern formed in the Pag anticline, which grew by buckling in shallow burial conditions. A major role in controlling final fold geometry and paleofluid flow is played by two misoriented transversal sets of low-displacement strike-slip faults, and by their interaction with subsidiary fold accommodation structures. The presence and, particularly, the abundance of such deformation features are difficult to constrain in seismic reflection datasets because of the low displacement values. We, consequently, stress the importance of studying appropriate field analogues by multiscale and multidisciplinary approaches, for the comprehensive understanding of fault-fold interaction, and the associated incremental deformation patterns.

ACKNOWLEDGMENTS

Discussions with Fabrizio Balsamo and Luigi Berio in the NEXT research group framework, are gratefully acknowledged. We are also indebted to Roberto Fantoni (Eni S.p.A.) for sharing his view on the tectonostratigraphic evolution of the External Dinarides. We are grateful to Enrico Selmo for

providing carbon and oxygen isotope data and discuss their significance, and to Andrea Comelli for providing thin sections. Technical support from Cristian Cavozi and Luca Barchi is gratefully acknowledged. The research has benefited from the equipment and framework of the COMP-HUB Initiative, funded by the ‘Departments of Excellence’ program of the Italian Ministry for Education, University and Research (MIUR, 2018–2022) to the University of Parma and from the donation of 10 Move IPM academic licenses to the University of Modena and Reggio Emilia. We are also grateful to Eni S.p.A. for funding this research and releasing the material for publication.

DATA AVAILABILITY STATEMENT

Structural data and coordinates of structural sites presented in this study are available in the Table S1 and S2 in the Supplementary Material and the Mendeley Data repository (<https://data.mendeley.com/datasets/ry7cy2k7hb/1>). There are no restrictions to this data usage.

AUTHOR CONTRIBUTIONS:

Conceptualization: LA, MS, SA, BA, MM, SF

Data curation: LA, MS, SA

Funding acquisition: BA, SF

Investigation: LA, MS, SA, BA, MM, SF

Methodology: LA, MS, SA, BA, SF

Project Administration: MM

Writing – original draft: LA, MS, SA, SF

Writing – review & editing: LA, MS, BA, MM, SF

BIBLIOGRAPHY

- Allan, J.R., & Matthews, R.K. (1982). Isotopic signatures associated with early meteoric diagenesis. *Sedimentology*, v. 29, p. 797–817. <https://doi.org/10.1111/j.1365-3091.1982.tb00085.x>.
- Angelier, J., & Mechler, P. (1977). Sur une methode graphique de recherche des contraintes principales egalement utilisables en tectonique et en seismologie: la methode des diedres droits. *Bull. Soc. Géol. de France*, S7-XIX, p. 1309–1318.
- Angelier, J., (1990). Inversion of field data in fault tectonics to obtain the regional stress - III. A new rapid direct inversion method by analytical means. *Geophys. J. Int.*, v. 103, p. 363–376. <https://doi.org/10.1111/j.1365-246X.1990.tb01777.x>.
- Babić, L., Zupanić, J., & Crnjaković, M. (1993). An association of marine tractive and gravity flow sandy deposits in the Eocene of the Island of Pag (Outer Dinarides, Croatia). *Geologia Croatica*, v. 46, p. 107–123.
- Babić, L. & Zupanić, J. (2007). Major events and stages in the Paleogene Promina Basin (Dinarides, Croatia). *Natura Croatica*, v. 16, p. 215–232.
- Babić, L. & Zupanić, J. (2008). Major events and stages in the sedimentary evolution of the Paleogene Promina basin (Dinarides, Croatia). *Geologia Croatica*, v. 16, no. 4, p. 215–232.
- Babić, L. & Zupanić, J. (2016). The youngest stage in the evolution of the Dinaric Carbonate Platform: the Upper Nummulitic Limestones in the North Dalmatian foreland, Middle Eocene, Croatia. *Natura Croatica*, v. 25/1, p. 55–71.

This article is protected by copyright. All rights reserved.

- Balling, P., Grützner, C., Tomljenovic, B., Spakman, W., & Ustaszewski, K. (2021a). Postcollisional mantle delamination in the Dinarides implied from staircases of Oligo-Miocene uplifted marine terraces. *Sci. Rep.*, v. 11, 2685. <https://doi.org/10.1038/s41598-021-81561-5>.
- Balling, P., Tomljenović, B., Schmid, S.M., & Ustaszewski, K. (2021b). Contrasting along-strike deformation styles in the central external Dinarides assessed by balanced cross-sections: implications for the tectonic evolution of its Paleogene flexural foreland basin system. *Glob. Planet. Chang.*, v. 205, 103587.
- Beaudoin, N.E., Lacombe, O., Hoareau, G., & Callot, J.P. (2022). How the geochemistry of syn-kinematic calcite cement depicts past fluid flow and assists structural interpretations: a review of concepts and applications in orogenic forelands. *Geological Magazine*, v. 159 (11-12), p. 2157-2190.
- Belinić, T., Kolínský, P., Stipčević J., & the AlpArray Working Group (2021). Shear-wave velocity structure beneath the Dinarides from the inversion of Rayleigh-wave dispersion. *Earth Planet. Sci. Lett.*, v. 555, 116686. <https://doi.org/10.1016/j.epsl.2020.116686>.
- Bennett, R.A., Hreinsdóttir, S., Buble, G., Bašić, T., Marjanović, M., Casale, G., Gendaszek, A., & Cowan, D. (2008). Eocene to present subduction of southern Adria mantle lithosphere beneath the Dinarides. *Geology*, v. 36, p. 3-6.
- Berio, L.R., Storti, F., Balsamo, F., Mittempergher, S., Bistacchi, A., & Meda, M. (2021). Structural Evolution of the Parmelan Anticline (Bornes Massif, France): Recording the Role of Structural Inheritance and Stress Field Changes on the Finite Deformation Pattern. *Tectonics*, v. 40, e2021TC006913. <https://doi.org/10.1029/2021TC006913>.
- Biot, M. A. (1965). Further development of the theory of internal buckling of multilayers. *Geological Society of America Bulletin*, 76(7), 833-840.
- Bistacchi, A., Massironi, M., Menegon, L., Bolognesi, F., & Donghi, V. (2012). On the nucleation of non-Andersonian faults along phyllosilicate-rich mylonite belts. Geological Society, London, Special Publications, 367(1), 185-199. <https://doi.org/10.1144/SP367.13>.
- Blašković, I. (1998). The two stages of structural formation of the coastal belt of the External Dinarides. *Geologia Croatica*, v. 51, p. 75-89.
- Blašković, I. (2005). Geologija Vinodola (Geology of Vinodol). – In: Biondić, R., Vlahović, I. & Velić, I. (eds.): 3. Hrvatski geološki kongres (Third Croatian Geological Congress), Vodič ekskurzija (Excursion Guide-Book), 39–48, Zagreb.
- Blay, P., Cosgrove, J. W., & Summers, J. M. (1977). An experimental investigation of the development of structures in multilayers under the influence of gravity. *Journal of the Geological Society*, 133(4), 329-342.
- Brlek, M., & Glumac, B. (2014). Stable isotopic ($\delta^{13}\text{C}$ and $\delta^{18}\text{O}$) signatures of biogenic calcretes marking discontinuity surfaces: a case study from Upper Cretaceous carbonates of central Dalmatia and eastern Istria, Croatia. *Facies*, v. 60, no. 3, p. 773-788.
- Brlek, M., Korbar, T., Košir, A., Glumac, B., Grizelj, A., & Otoničar, B. (2014). Discontinuity surfaces in Upper Cretaceous to Paleogene carbonates of central Dalmatia (Croatia): Glossifungites ichnofacies, biogenic calcretes and stratigraphic implications. *Facies*, v. 60, p. 467-487.
- Bulić, J., & Jurišić-Polšak, Z. (2009). Macropalaeontology and stratigraphy of lacustrine Miocene deposits at Crnika beach on the Island of Pag (Croatia). *Geologia Croatica*, v. 62, no. 3, p. 135-155. <https://doi.org/10.4154/gc.2009.16>.
- Burberry, C.M., & Swiatlowski, J.L. (2016). Evolution of a foldthrust belt deforming a unit with pre-existing linear asperities: insights from analog models. *Journal of Structural Geology*, v. 87, p. 1-18.
- Burkhard, M. (1993). Calcite twins, their geometry, appearance and significance as stress-strain markers and indicators of tectonic regime: a review. *Journal of structural geology*, v. 15, p. 351-368.
- Butler, R.W.H. (1989). The influence of pre-existing basin structure on thrust system evolution in the western Alps, in *Inversion Tectonics*, edited by Cooper, M.A., and Williams, G.D., *Geological Society of London, Special Publication*, v. 44, p. 105-122.
- Butler, R. W., Bond, C. E., Cooper, M. A., & Watkins, H. (2018). Interpreting structural geometry in fold-thrust belts: Why style matters. *Journal of Structural Geology*, 114, 251-273.
- Butler, R. W., Bond, C. E., Cooper, M. A., & Watkins, H. (2020). Fold-thrust structures—where have all the buckles gone?. Geological Society, London, Special Publications, 487(1), 21-44.
- Cannon, S. (2018). Reservoir modelling: A practical guide. John Wiley & Sons.

- Cerchiari, A., Remitti, F., Mitterpergher, S., Festa, A., Lugli, F., & Cipriani, A. (2020). Cyclical variations of fluid sources and stress state in a shallow megathrust-zone mélange. *Journal of the Geological Society*, v. 177(3), p. 647-659.
- Chorowicz, J. (1974). Le chevauchement du Velebit (Croatie, Yougoslavie). *Bulletin de la Societe Geologique de France*, v. 7/16, p. 74-85.
- Cooper, M. (1992). The analysis of fracture systems in subsurface thrust structures from the Foothills of the Canadian Rockies. *Thrust tectonics*, p. 391-405.
- Corbett, K., Friedman, K., & Spang, J. (1987). Fracture development and mechanical stratigraphy of Austin Chalk, Texas. *American Association of Petroleum Geosciences*, v. 71, p. 17-28.
- Ćosović, V., Drobne, K., & Moro, A., (2004). Paleoenvironmental model for Eocene foraminiferal limestones of the Adriatic carbonate platform (Istrian Peninsula). *Facies*, v. 50, p. 61-75.
- Ćosović, V., Mrinjek, E., Nemeč, W., Španiček, J., & Terzić, K. (2017). Development of transient carbonate ramps in an evolving foreland basin: *Basin Research*, v. 30, p. 746-765. <https://doi.org/10.1111/bre.12274>.
- Cox, S.F. (2010). The application of failure mode diagrams for exploring the roles of fluid pressure and stress states in controlling styles of fracture-controlled permeability enhancement in faults and shear zones. *Geofluids*, v. 10(1-2), p. 217-233.
- Davey, S.D., & Jenkyns, H.C. (1999). Carbon-isotope stratigraphy of shallow-water limestones and implications for the timing of Late Cretaceous sea-level rise and anoxic events (Cenomanian-Turonian of the peri-Adriatic carbonate platform, Croatia). *Eclogae Geologicae Helveticae*, v. 92, no. 2, p. 163-170.
- De Graaf, S., Nooitgedacht, C.W., Le Goff, J., Van der Lubbe, H.J.L., Vonhof, H.B., Reijmer, J.J.G. (2019). Fluid flow evolution in the Albanide fold-and-thrust belt: insights from $\delta^2\text{H}$ and $\delta^{18}\text{O}$ isotope ratios of fluid inclusions. *AAPG Bull.*, v. 103(10), p. 2421-2445. <https://doi.org/10.1306/02151918034>.
- de Leeuw, A., Mandić, O., Krijgsman, W., Kuiper, K., & Hrvatović, H. (2012). Paleomagnetic and geochronologic constraints on the geo-dynamic evolution of the Central Dinarides. *Tectonophysics*, v. 530-531, p. 286-298.
- Delvaux, D., & Sperner, B. (2003). New aspects of tectonic stress inversion with reference to the TENSOR program. *Geol. Soc. Lond., Spec. Publ.*, v. 212, p. 75-100. <https://doi.org/10.1144/GSL.SP.2003.212.01.06>.
- Dewey, J.F., Helman, M.L., Turco, E., Hutton, D.H.W., & Knott, S.D. (1989). Kinematics of the western Mediterranean, in *Alpine Tectonics*, *Geol. Soc. Spec. Publ.*, vol. 45, pp. 265-283, edited by Coward, M.P., Dietrich, D., & Park, R.G., Geol. Soc. of London, U.K.
- Dickson, J.A.D. (1966). Carbonate identification and genesis as revealed by staining. *Journal of Sedimentary Research*, v. 36, no. 2, p. 491-505.
- Diñçer, F. (2016). Eocene benthic foraminiferal assemblages from Central Anatolia (Turkey). Biostratigraphy, stable isotope data, paleoenvironmental and paleontological interpretations. *Journal of Asian Earth Sciences*, v. 114, p. 143-157.
- Dolan, J.F., & Avouac, J.P. (2007). Introduction to special section: Active fault-related folding: Structural evolution, geomorphologic expression, paleoseismology, and seismic hazards. *Journal of Geophys. Research: Solid Earth*, v. 112 (B3). <https://doi.org/10.1029/2007JB004952>.
- Dubey, A. K., & Cobbold, P. R. (1977). Noncylindrical flexural slip folds in nature and experiment. *Tectonophysics*, 38(3-4), 223-239.
- Dragičević, I., & Velić, I. (2002). The northeastern margin of the Adriatic Carbonate Platform. *Geol. Croatica*, v. 55/2, p. 185-232.
- Đurasek, N., Frank, G., Jenko, K., Kuzina, A., & Tonic-Gregl, R. (1981). Contribution of the understanding of oil-geological relations in NW Adriatic area. *Proceed. I Symp. scient. Conseil for oil. Jugosl. akad. znan. Umjetn. (A)*, 8, p. 201-213, Zagreb.
- Ellero, A., Ottria, G., Malusà, M.G., & Ouanaimi, H. (2012). Structural geological analysis of the High Atlas (Morocco): Evidences of a transpressional fold-thrust belt. In: Sharkov, E. (ed.) *Tectonics-Recent Advances*. In Tech, Rijeka, p. 229-258. <http://dx.doi.org/10.5772/50071>.
- Epard, J.L., & Groshong, R.Jr. (1993). Excess area and depth to detachment. *AAPG Bull.*, v. 77, p. 1291-1302.
- Erslev, E. A. (1991). Trishear fault-propagation folding. *Geology*, 19(6), 617-620.
- Evans, M.A., & Fischer, M.P. (2012). On the distribution of fluids in folds: a review of controlling factors and processes. *Journal Structural Geology*, v. 44, p. 2-24.

- Faivre, S. (2007). Analyses of the Velebit Mountain Ridge Crests. *Hrvatski geografski glasnik*, v. 69 (2), p. 21-40.
- Fischer, M.P., & Jackson, P.B. (1999). Stratigraphic controls on deformation patterns in fault related folds: a detachment fold example from the Sierra Madre Oriental, northeast Mexico. *Journal of Structural Geology*, v. 21, no. 6, p. 613-633.
- Friedman, I., & O'Neil, J.R. (1977). Compilation of stable isotope fractionation factors of geochemical interest, v. 440, *US Government Printing Office*.
- Ghosh, S.K. (1968). Experiments of buckling of multilayers which permit interlayer gliding. *Tectonophysics*, v. 6(3), p. 207-249.
- Grandić, S., Veseli, V., & Kolbah, S. (2002). Hydrocarbon potential of Dugi otok basin in offshore Croatia. *Nafta (Zagreb)*, v. 53/6-7, p. 215-224.
- Grandić, S. and Kolbah, S. (2009). New commercial oil discovery at Rovesti Structure in South Adriatic and its importance for Croatian part of Adriatic Basin. *Nafta*, v. 60, p. 68-82.
- Gross, M.R. (1993). The origin and spacing of cross joints: examples from the Monterey Formation, Santa Barbara Coastline, California. *Journal of Structural Geology*, v. 15, no. 6, p. 737-751.
- Gušić, I. & Jelaska, V. (1990): Stratigrafija gornjokrednih naslaga otoka Brača uokviru geodinamske evolucije Jadranske karbonatne platforme (Upper Cretaceous stratigraphy of the Island of the Brač). *Jugosl. akad. znan. i umjet., Institut zageološka istraživanja, OOUR za geologiju, str. 160*, Zagreb
- Gušić, I., & Jelaska, V. (1993). Upper Cenomanian–Lower Turonian sea-level rise and its consequences on the Adriatic–Dinaric carbonate platform. *Geol. Rundsch.*, v. 82/4, p. 676-686.
- Handy, M.R., Ustaszewski K., & Kissling, E. (2015). Reconstructing the Alps–Carpathians–Dinarides as a key to understanding switches in subduction polarity, slab gaps and surface motion. *Int. J. Earth Sci.*, v. 104, p. 1-26.
- Herak, M. (1999). Tectonic Interrelation of the Dinarides and the Southern Alps. *Geol. Croat., (Zagreb)* 52/1, p. 83-98.
- Hoefs, J. (1997). Stable Isotope Geochemistry (200 pp.). *Springer-Verlag*, Berlin.
- Holail, H. (1994). Carbon and oxygen ratios of Middle Eocene dolomite, Gebel Ataqa, Egypt. *Neues Jahrbuch für Geologie und Paläontologie. Abhandlungen*, v. 191, no. 1, p. 111-124.
- Honea, E., & Johnson, A. M. (1976). A theory of concentric, kink and sinusoidal folding and of monoclinial flexuring of compressible, elastic multilayers: IV. Development of sinusoidal and kink folds in multilayers confined by rigid boundaries. *Tectonophysics*, 30(3-4), 197-239.
- Howell, J.A., Martinius, A.W., Good, T.H. (2014). The application of outcrop analogues in geological modelling: a review, present status and future outlook. *Geological Society, London, Special Publications* 387 (1), 1. <https://doi.org/10.1144/SP387.12>.
- Hrvatovic, H. (2005). Geological guidebook through Bosnia and Hercegovina. *Geological Survey of Bosnia and Hercegovina*, Sarajevo.
- Ilić, A., & Neubauer, F. (2005). Tertiary to recent oblique convergence and wrenching of the Central Dinarides: constraints from a palaeostress study. *Tectonophysics*, v. 410, p. 465-484.
- ISIDE Working Group. (2007). Italian Seismological Instrumental and Parametric Database (ISIDE). Istituto Nazionale di Geofisica e Vulcanologia (INGV). <https://doi.org/10.13127/ISIDE>
- Ivančić, I., Herak, D., Herak, M., Allegretti, I., Fiket, T., Kuk, K., Markušić, S., Prevolnik, S., Sović, I., Dasović, I., and Stipčević, J. (2018). Seismicity of Croatia in the period 2006–2015. *Geofizika*, v. 35, p. 69-98.
- James, N.P., & Choquette, P.W. (1990). Limestones - the meteoric diagenetic environment. In: McIlreath, I.A., Morrow, D.W. (Eds.), Diagenesis. *Geosci. Can. Repr. Ser.*, v. 4, p. 35-73.
- Jamison, W. R. (1987). Geometric analysis of fold development in overthrust terranes. *Journal of structural Geology*, 9(2), 207-219.
- Jelaska, V., Gušić, I., Jurkovšek, B., Ogorelec, B., Čosović, V., Sribar, L. & Toman, M. (1994). The Upper Cretaceous geodynamic evolution of the Adriatic-Dinaric carbonate platform, in Proceedings, Perimediterranean carbonate platforms, First International Meeting: France, Marseille, 5-8 September 1994, Volume 21, p. 89-91.
- Johnson, K.M. (2018). Growth of fault-cored anticlines by flexural slip folding: Analysis by boundary element modeling. *Journal of Geophysical Research: Solid Earth*, v. 123, p. 2426–2447. <https://doi.org/10.1002/2017JB014867>.
- Kastelić, V., & Carafa, M.M.C. (2012). Fault slip rates for the active external Dinarides thrust-and-fold belt. *Tectonics*, v. 31, TC3019. <http://dx.doi.org/10.1029/2011TC003022>.

- Korbar, T. (2009). Orogenic evolution of the External Dinarides in the NE Adriatic region: a model constrained by tectonostratigraphy of Upper Cretaceous to Paleogene carbonates. *Earth-Science Reviews*, v. 96, no. 4, p.296-312. <https://doi.org/10.1016/j.earscirev.2009.07.004>.
- Korbar, T., Glumac, B., Tešović, B.C., & Cadieux, S.B. (2012). Response of a carbonate platform to the Cenomanian-Turonian Drowning and OAE 2: a case study from the Adriatic Platform (Dalmatia, Croatia). *Journal of Sedimentary Research*, v. 82, no. 3, p. 163-176. <https://doi.org/10.2110/jsr.2012/17>.
- Kovačević Galović, E., Ilijanić, N., Peh, Z., Miko, S., & Hasan, O. (2012). Geochemical discrimination of Early Palaeogene bauxites in Croatia. *Geologia Croatica*, v. 65 (1), p. 53–65.
- Kovačić, M. (2013). Geothermal properties of the northern part of the island of Rab. *Geologia Croatica*, v. 66(1), p. 29–37.
- Kovacs, I., Csontos, L., Szabò, Cs., Bali, E., Falus, Gy., Benedek, K., & Zajacz, Z. (2007). Paleogene–early Miocene igneous rocks and geodynamics of the Alpine–Carpathian–Pannonian–Dinaric region: an integrated approach. In: Beccaluva, L., Bianchini, G., Wilson, M. (Eds.), *Cenozoic volcanism in the Mediterranean area: Geological Society of America Special Paper*, v. 418, p. 93-112.
- Kuk, V., Prelogovic, E., & Dragicevic, I. (2000). Seismotectonically active zones in the Dinarides. *Geol. Croat.*, v. 53, p. 295-303.
- Lacombe, O. (2010). Calcite twins, a tool for tectonic studies in thrust belts and stable orogenic forelands. *Oil and Gas Science and Technology*, v. 65, no. 6, p. 809–838.
- Lacombe, O., Tavani, S., & Soto, R. (2012). An introduction to the Tectonophysics special issue “Into the deformation history of folded rocks”. *Tectonophysics*, v. 576–577, p. 1-3.
- Laubach, S.E., Eichhubl, P., Hilgers, C., & Lander, R.H. (2010). Structural diagenesis. *Journal of Structural Geology*, v. 32, no. 12, p. 1866-1872. <https://doi.org/10.1016/j.jsg.2010.10.001>.
- Le Breton, E., Handy, M.R., Molli, G., & Ustaszewski, K. (2017). Post-20 Ma Motion of the Adriatic Plate: new Constraints from Surrounding Orogens and Implications for Crust-Mantle Decoupling. *Tectonics*, v. 36, p. 3135-3154.
- Leever, K.A., Gabrielsen, R.H., Faleide, J.I., & Braathen, A. (2011). A transpressional origin for the West Spitsbergen fold-and-thrust belt: insight from analog modeling. *Tectonics*, v. 30, TC2014. <https://doi.org/10.1029/2010TC002753>.
- Lefticariu, L., Perry, E.C., Fischer, M.P., & Banner, J.L. (2005). Evolution of fluid compartmentalization in a detachment fold complex. *Geology*, v. 33, p. 69-72.
- Lehner, M., Tichler, L., Steinmüller, H., & Koppe, M. (2014). Power-to-Gas: Technology and Business Models, *Springer*. <http://dx.doi.org/10.1016/j.egypro.2014.11.836>.
- Linzer, H.-G., Ratschbacher, L., & Frisch, W. (1995). Transpressional collision structures in the upper crust: the fold-thrust belt of the Northern Calcareous Alps. *Tectonophysics* v. 242, p. 41-61.
- Macedo, J., & Marshak, S. (1999). Controls on the geometry of fold-thrust belt salients. *Geological Society of America Bulletin*, v. 111, no. 12, p. 1808-1822.
- Majcen, Ž., Korolija, B., Sokač, B., & Nikler, L. (1976). Osnovna geološka karta SFRJ 1:100 000. Tumač za list Zadar L 33-139. Institut za geološka istraživanja, Zagreb, *Savezni geološki zavod, Beograd*.
- Mamužić, P., & Sokač B. (1973). Osnovna geološka karta SFRJ 1:100 000. Tumač za listov Silba L 33-126 i Molat L 33-138. Institut za geološka istraživanja, Zagreb, *Savezni geološki zavod, Beograd*.
- Mandic, O., de Leeuw, A., Bulić, J., Kuiper, K.F., Krijgsman, W., & Jurišić-Polšak, Z. (2012). Paleogeographic evolution of the Southern Pannonian Basin: 40Ar/39Ar age constraints on the Miocene continental series of Northern Croatia. *International Journal of Earth Sciences*, v. 101, no. 4, p. 1033-1046. <https://doi.org/10.1007/s00531-011-0695-6>.
- Marshak, S. (1988). Kinematics of orocline and arc formation in thin-skinned orogens. *Tectonics*, v. 7, no. 1, p. 73-86.
- Márton, E., Drobne, K., Čosović, V., & Moro, A. (2003). Palaeomagnetic evidence for Tertiary counterclockwise rotation of Adria. *Tectonophysics*, v. 377, p. 143-156.
- Márton, V., Čosović, D., Bucković, & Moro, A. (2010). The tectonic development of the Northern Adriatic region constrained by Jurassic and Cretaceous paleo-magnetic results. *Tectonophysics*, v. 490, p. 93-102. <https://doi.org/10.1016/j.tecto.2010.04.032>.
- Márton, E., Čosović, V., & Moro, A. (2014). New stepping stones, Dugi otok and Vis islands, in the systematic paleomagnetic study of the Adriatic region and their significance in evaluations of existing tectonic models. *Tectonophysics*, v. 611, p. 141-154. <https://doi.org/10.1016/j.tecto.2013.11.016>.

- Márton, E., Čosović, V., & Moro, A. (2022). Changing directions of the tectonic structures, consistent paleomagnetic directions at the NE imbricated margin of Stable Adria. *Tectonophysics*, v. 843, 229594. <https://doi.org/10.1016/j.tecto.2022.229594>.
- Mazzoli, S., Basilici, M., Spina, V., Pierantoni, P. P., & Tondi, E. (2022). Space and time variability of detachment versus ramp-dominated thrusting: Insights from the outer Albanides. *Tectonics*, 41, e2022TC007274. <https://doi.org/10.1029/2022TC007274>.
- McKenzie, D.P. (1978). Active tectonics of the Alpine-Himalayan belt: The Aegean Sea and surrounding regions. *Geophys. J.R. Astron. Soc.*, v. 55, p. 217-254.
- Merlini, S., Doglioni, C., & Ponton, M. (2002). Analisi strutturale lungo un profilo geologico tra la linea Fella-Sava e l'avampaese adriatico (Friuli Venezia Giulia-Italia). *Memorie della Società Geologica Italiana*, v. 87, p. 31-40.
- Mitra, S. (2002). Fold accommodation faults. *AAPG Bulletin*, v. 86(9), p. 1673-1694.
- Mitterpergher, S., Succo, A., Bistacchi, A., Storti, F., Bruna, P.O. & Meda, M. (2019). Geological and structural map of the south-eastern Pag Island, Croatia: field constraints on the Cretaceous-Eocene evolution of the Dinarides foreland. *Geological Field Trips and Maps*, v. 11(2.4). <https://doi.org/10.3301/GFT.2019.04>.
- Morley, C. K. (1994). Fold-generated imbricates: examples from the Caledonides of Southern Norway. *Journal of Structural Geology*, 16(5), 619-631.
- Mrinjek, E. (1993). Sedimentology and depositional setting of alluvial Promina beds in northern Dalmatia, Croatia. *Geol. Croatica*, v. 46(2), p. 243-261.
- Muchez, P., Slobodnik, M., Viaene, W.A. & Keppens, E. (1995). Geochemical constraints on the origin and migration of palaeofluids at the northern margin of the Variscan foreland, southern Belgium. *Sedimentary Geology*, v. 96, no. 3-4, p. 191-200.
- Nabavi, S.T. & Fossen, H. (2021) Fold geometry and folding – a review. *Earth-Science Reviews* 222, 103812. <https://doi.org/10.1016/j.earscirev.2021.103812>
- O'Neil, J.R., Clayton, R.N. & Mayeda, T.K. (1969). Oxygen isotope fractionation in divalent metal carbonates. *J. Chem. Phys.*, v. 51, p. 5547-5558.
- Palenik, D., Matičec, D. Fuček, L., Matoš, B., Herak, M., Vlahović, I. (2019) Geological and structural setting of the Vinodol Valley (NW Adriatic, Croatia): insights into its tectonic evolution based on structural investigations. *Geologia Croatica* 72(3), 179-193. DOI: 10.4154/gc.2019.13
- Pamić, J., Gušić, I., & Jelaska, V. (1998). Geodynamic evolution of the Central Dinarides. *Tectonophysics*, v. 297, p. 251-268.
- Pavasović, M., Đapo, A., Marjanović, M., Pribičević, B. (2021). Present Tectonic Dynamics of the Geological Structural Setting of the Eastern Part of the Adriatic Region Obtained from Geodetic and Geological Data. *Appl. Sci.*, v. 11, 5735. <https://doi.org/10.3390/app11125735>.
- Persico, D., Succo, A., Storti, F., Piccinini, E., & Villa, G. (2019). Calcareous nannofossil biostratigraphy of the External Dinarides Flysch (Vrčić-Staravasa Pag Island, Croatia): A key to an Eocene tectono-stratigraphic and paleoenvironmental interpretation. *Geological Journal*, v. 55(6), p. 4656-4669. <https://doi.org/10.1002/gj.3673>.
- Piccoli, G., & Proto Decima, F. (1969). Ricerche biostratigrafiche sui depositi flyschoidi della regione Adriatica settentrionale e orientale. *Mem. Istituti di Geologia e Mineralogia dell'Università di Padova*, v. 27, p. 3-21.
- Picha, F.J. (2002). Late orogenic strike-slip faulting and escape tectonics in the frontal Dinarides-Hellenides, Croatia, Yugoslavia, Albania, and Greece. *AAPG Bulletin*, v. 86, p. 1659-1671.
- Placer, L., Vrabec, M., & Celarc, B. (2010). The bases for understanding of the NW Dinarides and Istria Peninsula tectonics. *Geologija*, v. 53 (1), 55-86.
- Prelogović, E., Kuk, V., & Buljan, R. (1998). The structural fabric and seismotectonic activity of northern Velebit: some new observations. *Rudarsko-geološki-naftni zbornik*, v. 10, p. 39-42.
- Price, N. J., & Cosgrove, J. W. (1990). Analysis of geological structures. Cambridge University Press.
- Ramsay, J. G. (1967). Folding and fracturing of rocks. Mc Graw Hill Book Company, 568.
- Ramsay, J. G. (1981). Tectonics of the Helvetic Nappes. Geological Society, London, Special Publications, 9(1), 293–309. [doi:10.1144/gsl.sp.1981.009.01.26](https://doi.org/10.1144/gsl.sp.1981.009.01.26).
- Rosenbaum, G., & Lister, G.S. (2002). Reconstruction of the evolution of the Alpine-Himalayan orogen - An introduction. *J. Virtual Explorer*, v. 8, p. 1-2.
- Roure, F., Swennen, R., Schneider, F., Faure, J.L., Ferket, H., Guilhaumou, N., Osadetz, K., Robion, P., & Vandeginste, V. (2005). Incidence and importance of tectonics and natural fluid migration on reservoir

- evolution in foreland fold-and-thrust belts. In: Brosse, E. (Ed.), *Oil and Gas Science and Technology, Oil and Gas Science and Technology. Revue de l'IFP* 60, p. 67–106.
- Salvini, F. (2019). Daisy3, the Structural Data Integrated System Analyzer, Software, version 5.38 [Software].
- Schmid, S., Bernoulli, D., Fugenschuh, B., Matenco, L., Schefer, S., Schuster, R., Tischler, M., & Ustaszewski, K. (2008). The Alpine-Carpathian-Dinaridic orogenic system: correlation and evolution of tectonic units. *Swiss Journal of Geosciences*, v. 101, no. 1, p. 139-183. <https://doi.org/10.1007/s00015-008-1247-3>.
- Shaw, J.H., Connors, C. & Suppe, J. (2005). Seismic Interpretation of Contractional Fault-Related Folds. *AAPG*, v. 53. <https://doi.org/10.1306/St531003>.
- Sinclair, H.D. (1997). Tectonostratigraphic model for underfilled peripheral foreland basins: an Alpine perspective. *Geological Society of America Bulletin*, v. 109 (3), p. 324-346.
- Sokač, B., Šcavničar, B., & Velić, I. (1976). Osnovna Geološka Karta SFRJ 1:100 000. Tumač za List Gospić L 33-127, Institut za geološka istraživanja: Zagreb, Croatia; *Savezni geološki zavod: Beograd*.
- Sperner, B., & Zweigel, P. (2010). A plea for more caution in fault-slip analysis. *Tectonophysics*, v. 482, p. 29–41. <https://doi.org/10.1016/j.tecto.2009.07.019>.
- Stearns, D.W. (1968). Certain aspects of fracture in naturally deformed rocks. *Rock Mechanics Seminar: Air Force Cambridge Research Laboratory*, p. 97-118.
- Storti, F., & Salvini, F. (1996). Progressive rollover fault-propagation folding: a possible kinematic mechanism to generate regional-scale recumbent folds in shallow foreland belts. *AAPG*, v. 80, no. 2, p. 174–193.
- Storti, F., Balsamo, F., Mozafari, M., Koopman, A., Swennen, R., & Taberner, C. (2018). Syn-Contractional Overprinting Between Extension and Shortening Along the Montagna Dei Fiori Fault during Plio-Pleistocene Antiformal Stacking at the Central Apennines Thrust Wedge Toe. *Tectonics*, v. 37, no. 10, p. 3690-3720.
- Šumanovac, F., Markušić, S., Engelsfeld, T., Jurković, K., & Orešković, J. (2017). Shallow and deep lithosphere slabs beneath the Dinarides from teleseismic tomography as the result of the Adriatic lithosphere downwelling. *Tectonophysics*, v. 712–713, p. 523–541.
- Suppe, J. (1983). Geometry and kinematics of fault–bend folding. *American Journal of Sciences*, v. 283, no. 7, p. 684-721.
- Tari-Kovačić, V., & Mrinjek, E. (1994). The role of Palaeogene clastics in the tectonic interpretation of Northern Dalmatia (Southern Croatia). *Geologia Croatica*, v. 47, no. 1, p.127-138.
- Tari-Kovačić, V. (1997). The development of the Eocene platform carbonates from wells in the middle Adriatic off-shore area, Croatia. *Geologica Croatica*, v. 50/1, p. 33-48.
- Tari, V. (2002). Evolution of the northern and western Dinarides: a tectonostratigraphic approach. *EGU Stephan Mueller Special Publications 1, European Geosciences Union*, p. 223-236.
- Tavani, S., Storti, F., Fernández, O., Muñoz, J.A. & Salvini, F. (2006). 3-D deformation pattern analysis and evolution of the Añisclo anticline, southern Pyrenees. *Journal of Structural Geology*, v. 28, no. 4, p. 695-712.
- Tavani, S., Storti, F., Salvini, F., & Toscano, C. (2008). Stratigraphic versus structural control on the deformation pattern associated with the evolution of the Mt. Catria anticline, Italy. *Journal of Structural Geology*, v. 30, no. 5, p. 664-681.
- Tavani, S., Storti, F., Lacombe, O., Corradetti, A., Muñoz, J.A, and Mazzoli, S. (2015). A review of deformation pattern templates in foreland basin systems and fold-and-thrust belts: Implications for the state of stress in the frontal regions of thrust wedges. *Earth-Science Reviews*, v. 141, p. 82-104. <https://doi.org/10.1016/j.earscirev.2014.11.013>.
- Tavani, S., Parente, M., Vitale, S., Iannace, A., Corradetti, A., Bottini, C., ... & Mazzoli, S. (2018). Early Jurassic rifting of the Arabian passive continental margin of the Neo-Tethys. Field evidence from the Lurestan region of the Zagros fold-and-thrust belt, Iran. *Tectonics*, 37(8), 2586-2607.
- Tavarnelli, E. (1996). Tethyan heritage in the development of the Neogene Umbria-Marche fold-and-thrust belt, Italy: A 3D approach. *Terra Nova*, v. 8(5), p. 470-478. <https://doi.org/10.1111/j.1365-3121.1996.tb00772.x>.
- Tešović, B.C., Glumac, B., & Buckovic, D. (2011). Integrated biostratigraphy and carbon isotope stratigraphy of the Lower Cretaceous (Barremian to Albian) Adriatic-Dinaridic carbonate platform deposits in Istria, Croatia. *Cretaceous Research*, v. 32, p. 301-324.

- Teysier, C., Tikoff, B., & Markley, M. (1995). Oblique plate motion and continental tectonics. *Geology*, v. 23(5), p. 447-450.
- Tišljar, J., Vlahović, I., Velić, I., & Sokač, B. (2002). Carbonate platform megafacies of the Jurassic and Cretaceous deposits of the Karst Dinarides. *Geol. Croatica*, v. 55/2, p. 139-170.
- Traforti, A., Massironi, M., Bistacchi, A., Zampieri, D., & Viola, G. (2018). Slip-tendency analysis as a tool to constrain the mechanical properties of anisotropic rocks. *J. Struct. Geol.*, v. 117, p. 136–147. <https://doi.org/10.1016/j.jsg.2018.09.001>.
- Urych, T., Čečko, J., Magdziarczyk, M., Smoliński, A. (2022). Numerical Simulations of Carbon Dioxide Storage in Selected Geological Structures in North-Western Poland. *Front. Energy Res.*, v. 10, 827794.
- Ustaszewski, K., Schmid, S.M., Fügenschuh, B., Tischler, M., Kissling, E., and Spakman, W. (2008). A map-view restoration of the Alpine-Carpathian-Dinaridic system for the early Miocene. *Swiss J. Geosci.*, v. 101(suppl 1), p. 273-294.
- Van Unen, M., Matenco, L., Nader, F.H., Darnault, R., Mandic, O., & Demir, V. (2019) Kinematics of Foreland-vergent crustal accretion: inferences from the Dinarides evolution. *Tectonics*, v. 38, no. 1, p. 49-76. <https://doi.org/10.1029/2018TC005066>.
- Veizer, J., Ala, D., Azmy, K., Bruckschen, P., Buhl, D., Bruhn, F., & Jasper, T. (1999). $^{87}\text{Sr}/^{86}\text{Sr}$, $\delta^{13}\text{C}$ and $\delta^{18}\text{O}$ evolution of Phanerozoic seawater. *Chemical geology*, v. 161, no. 1-3, p. 59-88.
- Velić, I., Vlahović, I., & Matičec, D. (2002). Depositional sequences and palaeogeography of the Adriatic carbonate platform. *Mem. Soc. Geol. It.*, v. 57, p.141-151.
- Velić, I., Malvić, T., Cvetković, M., & Velić, I. (2015). Stratigraphy and petroleum geology of the Croatian part of the Adriatic Basin. *J. Pet. Geol.*, v. 38, p. 281-300. <https://doi.org/10.1111/jpg.12611>.
- Vlahović, I., Tišljar, J., Velić, I., & Matičec, D. (2002). The Karst Dinarides are composed of relics of a single Mesozoic platform: facts and consequences. *Geol. Croatica*, v. 55/2, p. 171-183.
- Vlahović I., Tišljar J., Velić I., & Matičec D. (2005). Evolution of the Adriatic Carbonate Platform: Palaeogeography, main events and depositional dynamics. *Palaeogeography and Palaeocology*, v. 220, no. 3–4, p. 333-360. <https://doi.org/10.1016/j.palaeo.2005.01.011>.
- Wennberg, O.P., Svånå, T., Azizzadeh, M., Aqrabi, A.M.M., Brockbank, P., Lyslo, K.B., & Ogilvie, S. (2006). Fracture intensity vs. mechanical stratigraphy in platform top carbonates: the Aquitanian of the Asmari Formation, Khaviz Anticline, Zagros, SW Iran. *Petroleum Geosciences*, v. 12, no. 3, p. 235-246.
- Žibret, L. & Vrabc, M. (2016). Palaeostress and kinematic evolution of the orogen-parallel NW-SE striking faults in the NW External Dinarides of Slovenia unraveled by mesoscale fault-slip data analysis. *Geol. Croatica*, v. 69/3, p. 295-305. DOI: 10.4154/gc.2016.30
- Salvini, F., & Storti, F. (2001). The distribution of deformation in parallel fault-related folds with migrating axial surfaces: comparison between fault-propagation and fault-bend folding. *Journal of Structural geology*, 23(1), 25-32.
- Gušić, I., & Jelaska, V. (1993). Upper Cenomanian-Lower Turonian sea-level rise and its consequences on the Adriatic-Dinaric carbonate platform. *Geologische Rundschau*, 82, 676-686.
- Berio, L. R., Mittempergher, S., Storti, F., Bernasconi, S. M., Cipriani, A., Lugli, F., & Balsamo, F. (2022). Open–closed–open palaeofluid system conditions recorded in the tectonic vein networks of the Parmelan anticline (Bornes Massif, France). *Journal of the Geological Society*, 179(5), jgs2021-117.

FIGURE CAPTIONS

This article is protected by copyright. All rights reserved.

Figure 1. Geological setting. (A) Sketch map indicating the location of the Dinarides thrust belt in the circum-Adriatic geodynamic context. (B) Tectono-stratigraphic map of the Dinarides (adapted from Van Unen et al., 2019 and modified from Schmid et al., 2008; Vlahović et al., 2005; Korbar, 2009). Red triangle and trace refer to locations of (c) and (d). (C) Enlargement of the tectono-stratigraphic context around the studied area, including Pag island, the Velebit Mts. and the Lika region in the northeast. Faults are in red; black dots indicate location of exploration wells Ravni Kotari 1 and 2; red rectangle encompasses the area of Fig. 3. (D) Cross-section (adapted from Grandić et al., 2002) from the central part of the Adriatic Sea in the southwest to the Split-Karlovac fault system in the northeast.

Figure 2. Stratigraphy of the Pag island. (A) Field picture of the Milna fm. showing multiple cycles of massive packstone and wackestone intercalated by stromatolitic layers. (B) Hardground stained by iron oxides and marked by bioturbation at the top of the Milna fm. (C) Outcrops showing Gornji Humac fm. characterized by alternations of white grainstones, packstones and greyish mudstones. Pen for scale. (D) Picture showing reddish paleosol at the top of the Gornji Humac fm. (E) Pictures illustrating facies types of the foraminiferal limestones, i.e., a lower wackestone sub-unit and an upper packstone one. (F) Picture shot looking southwards, showing the anticline forelimb north of Pag village; the sedimentary succession shown spans from the top of the foraminiferal limestones to the base of the Dalmatian flysch, transitioning through the transitional beds; tourists above marls for scale. (G) Photo, looking southeast, of poorly cemented, sandstone-rich beds of the Dalmatian flysch, outcropping on the southwest shore of the Paški zaljev, part of backpack for scale. (H) Detail of the Velebit breccia; photo taken northeast of Metajina village. (I) Outcrop picture showing coal-rich lacustrine sediments of the Crnika beach section, located on the southwest shore of Paški zaljev. (J) Schematic stratigraphic succession of Pag island; symbols of the sedimentary facies types are described in the lower part of the figure.

Figure 3. Geological map of the Pag and Poveljana anticlines from Mitterpergher et al. (2019) with traces of the geological cross sections shown in A to F, from NW to SE; β axis and π plane obtained from cumulative bedding pole density contours of the northwestern part (southeastern part and Poveljana) of the Pag anticline in blue (red) from our dataset (Schmidt lower hemisphere stereographic projection; contour interval 2%) are shown in the upper right corner of the map; rose diagram showing cumulative azimuth distribution of strike-slip faults from our dataset are shown on the left side of the map. (A-B-C-D-E-F) Geological cross-sections of the Pag anticline from NW to SE.

Figure 4. Orientation of the background deformation structures. Schmidt lower hemisphere stereoplots of the background deformation structures measured in the sites shown on a Schematic map of the Pag anticline and are colored based on lithostratigraphy. Stereographic projections are plotted on lower hemisphere, Schmidt net; pole density contours have intervals of 3% (in all figures). All structural elements are plotted both in their orientation (opaque stereonets) and after back-rotating bedding to horizontal (blue lined sharp stereonets).

Figure 5. Field pictures of background deformation structures. (A) Field photo of a vertical section of Gornji Humac fm. in the crest to forelimb transition showing bed-parallel vein exploiting bed-parallel burial stylolites and crosscut by transversal vein. (B) Association of axial-parallel stylolites and clustered cross-fold veins in the Gornji Humac fm.; map view. (C) Outcrop of foraminiferal limestones displaying the same structural association: mutually crosscutting axial-parallel pressure solution wavy cleavage and $V_{2F.L.}$ veins; map view. (D) Picture showing the top of a medium angle, NE dipping Dalmatian flysch sandstone bed,

where conjugate shear joints occur along with transversal joints and veins, and a third minor, discontinuous joint set, parallel to the bed strike on the right, which occurs along compaction bands. (E) Sketch of a bed surface of Gornji Humac fm. in the backlimb, back-rotated to the horizontal, showing a composite deformation pattern including two conjugate strike-slip vein arrays, orthogonal to bedding, a right-lateral NNE-SSW set (F) and left-lateral ENE-WSW set (G).

Figure 6. Field pictures of thrust structures. (A) Photo looking south highlighting the triangle zone defined by the main backthrust along the NE coast of Pag and by the subsidiary forethrust outcropping in the lower left corner of the image. (B) Outcrop picture shot looking SE, showing the subsidiary forethrust involving foraminiferal limestones above transitional beds cross-cut by a strike-slip fault zone. (C) Detail, looking NW, of the main backthrust illustrating pluridecametric thrust-related folds in both hanging wall and in the verticalized footwall strata. (D) Outcrop detail along a subsidiary thrust fault plane displaying both bed parallel veins and younger thrust related veins which dip towards the vergence direction of the associated thrust fault, e.g., towards SW here. Stereonets in (a) and in (d) show thrust faults in red and other structures are according to the legend of Fig. 4.

Figure 7. Field pictures of fold accommodation structures. (A) Field picture showing a forethrust in the backlimb, interpreted as an out-of-the-syncline thrust, and a roof backthrust at the transition with the crest. (B) Detail of the fault zone of the out-of-the-syncline thrust, composed of about 1 meter of cataclasite arranged in S-C shear lenses. (C) Photo showing a thrust bounding decameter-scale duplexes in the backlimb, with top-to the hinge (right in the picture) sense of transport; structural measurements are plotted separately for each sector. (D) Field photo of Site 5 in the backlimb where bedding dips at medium to high angle and is crosscut by meter-scale conjugated thrusts; the thrusts dipping towards the NE have a very high dip angle, suggesting that they formed when beds were still horizontal, and were exploited as strike-slip faults upon backlimb rotation. (E) Field image of the backlimb (NE) - crest (SW) transition, consisting of a volume of superimposed and indented duplexes in a fishtail structure. Backpack for scale. (F) NE-SW trending valley exposing the anticline nucleus formed of superimposed hectometric duplexes in Milna fm., crosscut by E-W strike-slip faults; person circled in red for scale.

Figure 8. (A) Field picture looking towards SE in site 21 showing sigmoidal partially bleached lenses formed subparallel to bedding during extensional soft-sediment deformation. (B) Sigmoidal, foliation-bounded soft sediment fault core lenses composed of compacted and cemented sub-rounded chaotic breccias. (C) Slumped beds in the damage zone of a ramp segment of the soft sediment extensional fault zone in site I. Orthophotomosaics of the architecture of soft-sediment faults in site 21 (D) and in site 22 (E); fault segments with soft-sediment deformation structures are colored in green, strike-slip faults are in red. Fault segment kinematics and reactivation are indicated in the legend. All the deformation structures are shown in the Schmidt lower hemisphere stereonet; bedding is in blue, faults in red, and pressure-solution cleavage planes in grey.

Figure 9. Orientations and field pictures of fault related deformation structures. (A) Schematic map of the Pag anticline with stratigraphic and structural lineaments as in Fig. 4. Sites are colored following lithostratigraphy. Legend shows elements in stereographic projections, which are plotted on lower hemisphere Schmidt stereonet. Faults represented in this image have strike-slip kinematics. (B) Field image of N-S striking right-lateral fault with reddish fault core in the Milna fm.; red line marks fault core-damage zone boundary; green and grey marks represent fault related veins and stylolites. (C) Detail of mutually crosscutting fault related N-S and roughly E-W (ENE-WSW) veins in the Gornji Humac. fm. (D) Outcrop detail of Gornji Humac fm. in the pericline area displaying mutually crosscutting N-S and E-W stylolites. (E) Field image showing the fault core of a left-lateral fault producing pluridecametric offset between the foraminiferal limestones and the Dalmatian flysch, in map view.

Figure 10. Petrography of carbonate cements. TSS stands for thin section scan; PPL for plane-polarized; CL for cathodoluminescence. (A) TSS of Milna fm. mudstones showing wavy laminated layers including peloids and algal mats. (B) Enlargement of A in CL illustrating calcitized idiopathic matrix dolomite crystals and V_3 vein formed by calcite crystals with well evident non-luminescent and yellow-orange growth zones. (C) PPL image of C_{topK} geopetal calcite, showing halos of growth zones that were not overprinted by recrystallization, cross-cut by V_1 calcite vein. (D) XPL detail of C_{late} calcite showing growth zones intercalated by silty, solid inclusion rich bands. (E, F) PPL and CL images of Dalmatian flysch showing the homogeneous orange-colored interparticle calcite cement. (G) TSS of Gornji Humac fm. showing crosscutting relationships between V_1 and V_2 veins; V_1 shows extremely twinned calcite crystals, V_2 is characterized by rims with solid inclusions zones and dissolution halos. (H) CL detail of C illustrating non-luminescent, highly twinned V_1 calcite crosscut by V_2 which is composed by a purplish calcite cement $V_2(d)$, replacing fracture-filling dolomite, visible by inclusion zone halos, and by orange calcite cement overgrowths $V_2(c)$. (I) PPL and (J) CL image showing part of V_2 *en échelon* vein crosscutting V_T vein; they are characterized by non-luminescent calcite cements with different twinning intensities. (K) PPL and (L) CL images of V_T veins, filled by intensely twinned non-luminescent calcite, crosscut by a non-twinned V_3 vein. (M) PPL and (N) CL microphotographs illustrating well preserved dolomite habit in $V_2(d)$, overgrown by $V_2(c)$ and later antitaxial fracturing of V_3 non-luminescent and yellow calcite cement. (O) PPL and (P) CL images of a V_{2FL} vein in the foraminiferal limestones; they are cemented by elongate-blocky to fibrous calcite with twinning Type I and have the same CL color of the host rock. (Q) TSS of the foraminiferal limestones including a V_{2FL} showing syntaxial re-opening by V_{3FL} . (R) Detail of (Q) showing CL of V_{3FL} , which looks dark orange and dull but preserve the distinct growth zones typical of V_3 .

Figure 11. Stable isotope geochemistry of host rocks and calcite cements. (A) Plot illustrating results of $\delta^{18}O\%$ vs. $\delta^{13}C\%$ of analyzed limestone host rocks and calcite cements. See legend above the plot for cement types with respect to stratigraphy and relative timing. HR are host rocks, V are vein cements, and C are other types of cements. Dashed green box indicated with K.SW shows the range of values of limestones which precipitated in equilibrium with Cenomanian to Coniacian seawater. (B) Plot illustrating mean and standard deviation values of the calcite cement types along with the diagenetic processes responsible for their evolution.

Figure 12. Summary of background and fault-related deformation structures. (A) Deformation structures summarized in a stratigraphy vs. relative timing framework. Cretaceous carbonates have been grouped in a single unit since they show consistent deformation patterns. (B) 3D block model showing deformation structures far from fault zones and schematic table indicating their crosscutting sequence; view orthogonal to bedding. (C) 3D block model illustrating deformation structures localized along fault zones.

Figure 13. Cartoon showing the proposed evolutionary steps for the deformation pattern of the Pag anticline. (A) Schematic representation of the nucleation of bed parallel veins V_1 and incipient conjugate thrust pairs associated with thrust-related veins V_T and tectonic stylolites striking parallel to the fold axis. (B) Progressive contraction caused buckle folding of the multilayer and the switch of σ_2 from sub-horizontal to sub-vertical, triggering the nucleation of V_2 transversal veins and associated stylolites. Transversal veins also formed *en échelon* arrays locally organized in incipient strike-slip deformation zones. (C) The V_3 pattern mostly developed along strike-slip fault zones and re-opened earlier structures; bed perpendicular stylolites, V_2 veins, and faults and veins along thrust faults reactivated with right-lateral strike-slip kinematics.

Figure 14. Simplified tectonic sketch showing the relations between the Pag anticline and fault zones: possible block rotations and interactions between thrusts in the pericline, and strike-slip faults along the fold.

Figure 15. Analysis of detachment depth. (A) Geological cross-section of Fig. 3E, adapted from [Mittempergher et al. \(2019\)](#). Detachment depth was calculated according to the excess area method of [Epard and Groshong \(1993\)](#). (B) Plot of excess area vs. depth of reference levels. Regression lines for the different anticlines shown in the cross-section intersect the horizontal axis at the calculated minimum detachment depth for that anticline. Horizontal axis reports depth from sea level datum; the reference level was set at -2 km depth.

Figure 16. Paleostress analysis. (A) Paleostress results derived by thrust related deformation structures are shown in red (prefolding) while results derived by inversion of transversal veins and longitudinal pressure solution planes are indicated in blue (synfolding); results are displayed with dashed margins when poorly constrained. (B) Paleostress results derived by inversion of structural elements localized along strike-slip faults (postfolding); results are displayed with dashed margins when poorly constrained. (C-D-E) Results of bootstrap statistics of tensors derived by inversion of structural data, respectively for thrusting (red), folding (blue) and postfold strike-slip faulting (orange).

Figure 17. Conceptual 3D block diagram showing the fluid types and their migration pathways in the study area. Timing and relative burial are also proposed. (A) Paleocene forebulge stage; (B) Early Eocene layer parallel shortening stage; (C) Late Eocene folding stage; (D) Oligocene postfolding stage.

Table 1. Calcite cement types and related $\delta^{18}\text{O}\%$ and $\delta^{13}\text{C}\%$ (V-PDB) ranges, mean and standard deviation values.

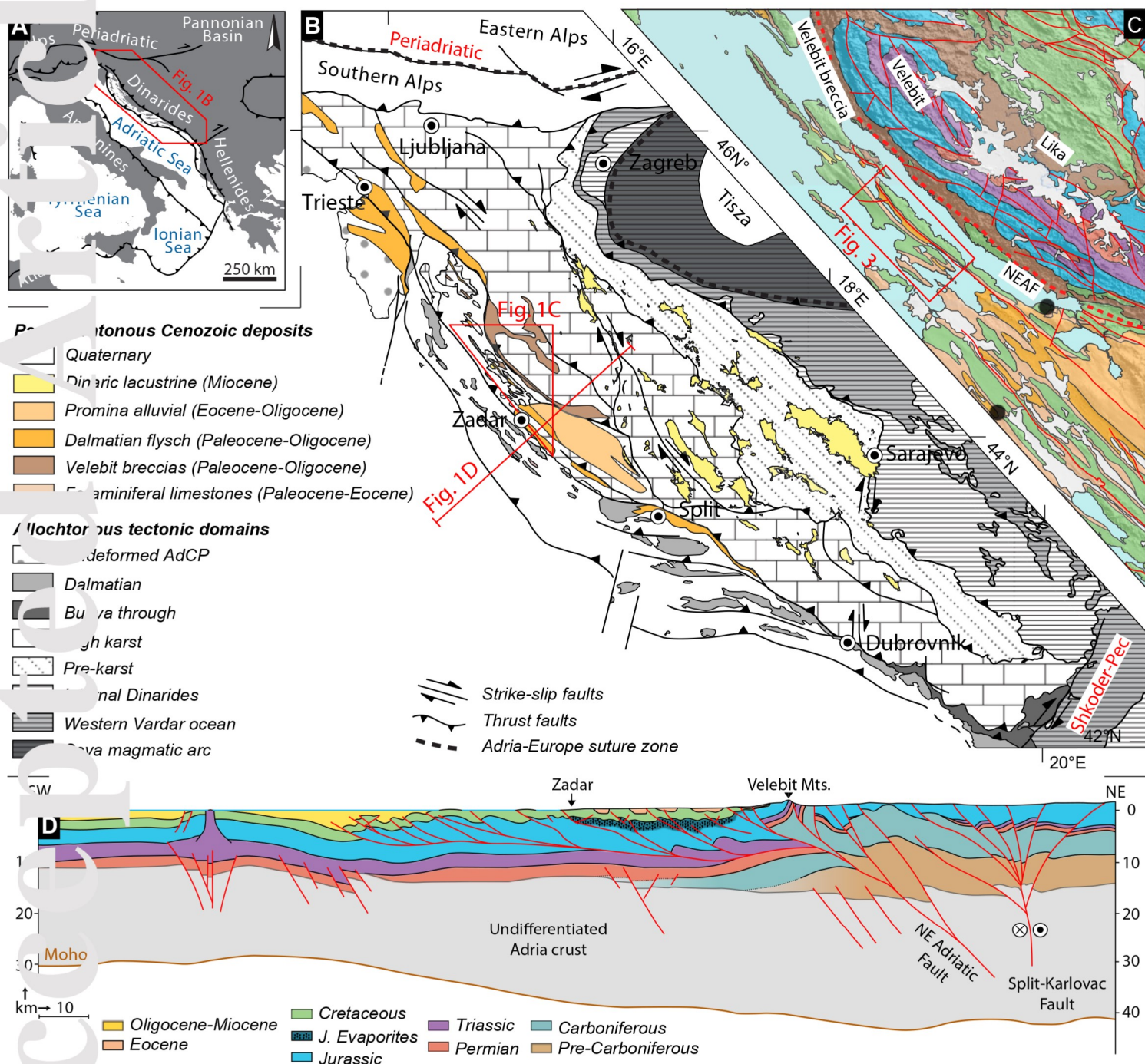
Table 2. Results of the paleostress analysis. Pl: plunge; Tr: trend; St. Dev: standard deviation; R: ratio of principal stresses differences; R': stress regime index; QRW: quality rank as defined by the World Stress Map Project; QRT: quality rank including parameters quantifying the diversity of input data.

Table 1. Stable Isotope Results of calcite cement types

Cement type	$\delta^{18}\text{O}\text{‰}$ (V-PDB)			$\delta^{13}\text{C}\text{‰}$ (V-PDB)		
	Range	Mean	St. dev. ($\pm 1\sigma$)	Range	Mean	St. dev. ($\pm 1\sigma$)
C_{late} (8)	-6.5 / -5.1	-5.77	0.39	-11.1 / -7.2	-9.19	1.08
V_{3F.L.} (14)	-6.5 / -4.7	-5.64	0.42	-5.9 / -2.1	-3.72	1.15
V₃ (53)	-6.7 / -4.7	-5.61	0.50	-7.3 / -0.7	-4.22	1.77
C_{D.F.} (10)	-5.3 / -3.3	-4.20	0.70	-1.1 / +1.9	-0.18	0.72
V_{2F.L.} (37)	-9.3 / -4.2	-5.92	1.14	-1.2 / +2.5	+0.91	0.95
V₂ (34)	-9.0 / -5.6	-7.57	0.65	-4.4 / +2.2	-1.15	1.96
V_T (20)	-7.3 / -4.5	-6.09	0.74	-1.1 / +1.5	+0.36	0.60
V₁ (3)	-6.6 / -4.6	-5.81	0.84	-0.7 / +0.3	-0.06	0.41
HR_{F.L.} (21)	-4.6 / -2.5	-3.43	0.56	-0.8 / +2.1	+1.16	0.77
C_{topK} (12)	-6.1 / -5.0	-5.42	0.28	-9.8 / -1.5	-6.03	2.39
HR_{topK} (12)	-6.2 / -4.4	-5.25	0.50	-7.1 / -2.6	-4.85	1.47
HR_{G.H.} (33/36)	-6.2 / -3.4	-4.63	0.75	-0.8 / +2.4	0.75	0.79
HR_{S.D.} (6/9)	-5.6 / -3.6	-4.50	0.83	+1.1 / +3.4	2.02	0.79
HR_{Milna} (6)	-5.5 / -3.5	-4.14	0.98	-0.3 / +3.1	1.66	1.02

Table 2. Results of paleostress analysis

Structures Site	σ_1 :Pl/Tr	St. Dev.	σ_2 :Pl/Tr	St. Dev.	σ_3 :Pl/Tr	St. Dev.	R	R'	St. Dev.	QRw	QRt	Used Data	Total Data	Used/Tot
THRUST_16_17	42/6	50.3	311/6	49.9	177/82	19.3	0.81	2.81	1.23	C	C	163	209	0.78
THRUST_18	45/4	16.3	314/18	42.2	147/71	41.8	0.11	2.11	0.19	C	D	103	103	1
THRUST_5	223/7	16.7	131/9	18.5	349/79	17	0.67	2.67	1.18	D	D	85	89	0.96
THRUST_6	228/10	30.8	136/8	31.2	8/77	17.1	0.85	2.85	1.25	D	D	115	157	0.73
BACKGR_4	212/1	10.9	313/87	23.7	122/3	22.6	0.28	1.72	0.34	D	D	43	75	0.57
BACKGR_13	200/12	14.1	64/74	18.8	292/11	15.3	0.44	1.56	0.81	C	C	38	44	0.86
BACKGR_12	59/18	17.6	212/70	19.8	326/9	12.5	0.68	1.32	0.73	C	C	98	127	0.77
BACKGR_1	60/21	16	266/67	21.8	154/9	21.2	0.38	1.62	0.83	D	D	43	43	0.84
BACKGR_8	260/19	14	41/66	17.1	165/14	13.7	0.57	1.43	0.77	C	C	106	117	0.91
BACKGR_7	54/15	13.8	207/73	18.3	322/7	15	0.46	1.54	0.8	C	C	193	202	0.96
BACKGR_11	205/20	14.6	354/67	18.5	111/11	14.9	0.47	1.53	0.8	D	D	37	51	0.73
BACKGR_10	237/7	9.4	332/37	49	138/52	49	0.04	2.04	0.96	C	E	68	94	0.72
BACKGR_3	54/24	14.9	202/63	17.9	318/12	13.1	0.59	1.41	0.76	C	C	128	138	0.93
BACKGR_2	66/84	39.1	222/5	39.4	312/2	9.7	0.77	0.77	0.58	C	D	30	37	0.81
BACKGR_5	43/2	11.3	291/85	14.2	133/4	13.5	0.32	1.68	0.85	C	C	70	79	0.89
BACKGR_14	61/8	16.8	216/82	18.8	330/3	12.4	0.72	1.28	0.72	C	C	48	54	0.89
BACKGR_15	214/2	12	112/83	19.3	305/7	17.9	0.29	1.71	0.85	C	C	146	152	0.96
S.S._FAULTS_4	87/74	26.8	191/4	27.3	282/15	13.2	0.78	0.78	0.58	E	E	56	77	0.73
S.S._FAULTS_13	63/13	14.9	304/65	19	158/21	15.7	0.27	1.73	0.35	C	C	122	167	0.73
S.S._FAULTS_12	11/12	26.3	132/67	26.7	277/19	10.7	0.8	1.2	0.7	C	C	46	50	0.92
S.S._FAULTS_1	252/4	17.8	2/79	19.1	161/10	13.3	0.27	1.73	0.25	D	D	85	104	0.82
S.S._FAULTS_20	250/30	49.4	78/60	49.6	342/4	16.4	0.8	1.2	0.7	D	D	35	41	0.85
S.S._FAULTS_7	5/4	14.9	108/73	19.4	274/16	15.2	0.19	1.81	0.12	D	E	80	312	0.26
S.S._FAULTS_9	192/18	33.6	52/67	33.6	286/14	8.9	1	1	0.64	C	E	50	57	0.88
S.S._FAULTS_19	36/2	12.9	281/86	34.2	126/4	33.4	0.18	1.82	0.89	D	D	127	180	0.71
S.S._FAULTS_11	9/7	46.5	138/80	48	278/8	19.3	0.69	1.31	0.73	C	C	62	96	0.65
S.S._FAULTS_3	19/30	16.2	154/51	19.4	275/23	16	0.39	1.61	0.82	C	C	123	124	0.99
S.S._FAULTS_20	57/2	27.6	289/87	28	147/3	13.7	0.83	1.17	0.69	C	D	33	37	0.89
S.S._FAULTS_18	246/21	37.3	61/69	33.6	156/2	41.8	0.75	1.25	0.71	D	E	177	215	0.82
S.S._FAULTS_6	103/19	35.4	232/61	36.1	6/21	11.4	0.85	1.15	0.68	D	D	12	30	0.4
S.S._FAULTS_14	40/8	21.6	282/73	28.1	132/15	21.3	0.35	1.65	0.16	C	C	66	83	0.8



This article has been accepted for publication and undergone full peer review but has not been through the copyediting, typesetting, pagination and proofreading process, which may lead to differences between this version and the [Version of Record](https://doi.org/10.1029/2023TC007781). Please cite this article as [doi: 10.1029/2023TC007781](https://doi.org/10.1029/2023TC007781).

This article is protected by copyright. All rights reserved.